

Momentum and kinetic energy transport in supersonic particle-laden turbulent boundary layers

Ming Yu,¹ Yibin Du,^{2,1} Qian Wang,^{3,1} Siwei Dong,¹ and Xianxu Yuan^{1,*}

¹*State Key Laboratory of Aerodynamics, Mianyang, 621000, China*

²*School of Aeronautic Science and Engineering,
Beihang University, Beijing, 100191, China*

³*Tianjin University, Tianjin 300072, China*

(Dated: July 1, 2024)

In the present study, we conduct direct numerical simulations of two-way force-coupled particle-laden compressible turbulent boundary layers at the free-stream Mach number of 2.0 for the purpose of examining the effects of particles on the transport of momentum and kinetic energy. By analyzing turbulent databases with various particle Stokes numbers and mass loadings, we observe that the presence of particles suppresses turbulent fluctuations and can even laminarize flow under high mass loading conditions. This is reflected by the wider and more coherent near-wall velocity streaks, reduced Reynolds stresses, and diminished contributions to skin friction and turbulent kinetic energy production. Additionally, the particle feedback force becomes more dominant in turbulent production near the wall and at small scales as mass loadings increase, which is found to be caused by the residual velocity fluctuations from particles swept down from the outer region. Furthermore, we identify that particle dissipation, resulting from the relative velocity between the fluid and particles, accounts for less than 1% of mean kinetic energy viscous dissipation and less than 10% of turbulent kinetic energy dissipation in the case with the highest mass loading. This suggests a modest impact on the internal energy variation of the fluid if two-way heat coupling is introduced. The elevated mean temperature is found in the near-wall region and is ascribed to the influence of the particle feedback force and reduced turbulent diffusion in high mass loading cases.

I. INTRODUCTION

Particle-laden wall-bounded turbulent flows are commonly encountered in nature and engineering applications [1–3]. The wall-bounded turbulent flows, characterized by a range of scales and containing energetic eddies whose sizes are influenced by their distances from the walls, carry the dispersed phase particles to acceleration and deceleration, to deposition and resuspension, to clustering and segregation [4–7]. In return, despite their small size, these particles impact turbulent motions by exerting feedback forces that extend to scales significantly larger than their own diameters [8]. The complexity of

* Corresponding author: yuanxianxu2023@163.com

these processes is further increased in the presence of flow compressibility, particularly in scenarios such as aerospace engineering where high-speed vehicles travel through extreme weather conditions [9, 10].

When the particles are significantly smaller than the smallest turbulence scale and the total volume fractions are low, particle-laden flows can be simulated using the Eulerian-Lagrangian point-particle method. In this method, turbulent fluid flows are treated as continuous phases simulated in the Eulerian coordinate system, while the motions of dilute phase particles are tracked in the Lagrangian frame [6, 8], which has been proven to be capable of replicating the experimental results [11, 12]. Despite such simplification, there are still multiple parameters affecting the statistics and dynamics of both the particles and turbulent fluid flows, including the Reynolds and Mach numbers from the perspective of the flows, and the particle inertia and mass loading from the perspective of particles. The particle inertia can be evaluated by the particle Stokes number, which is represented by the ratio between the particle response time τ_p and the characteristic time scale of the flow $St = \tau_p/\tau_f$. In wall-bounded turbulence, the characteristic timescale of the flow is commonly determined by the wall flow quantities, such as the wall shear stress τ_w , the wall viscosity μ_w and wall fluid density ρ_w , hereinafter referred to as St^+ . Mass loading, on the other hand, refers to the ratio between the mass of the particles M_p and the fluid M_f in the flow system $\varphi_m = M_p/M_f$. In the limit of low mass fraction, the impact of feedback forces from particles to the fluid can be neglected, resulting in one-way coupling where particles are solely transported by the fluid. It has been observed that in both incompressible and compressible wall-bounded turbulence [13, 14], light particles act as tracers, almost following the motions of the fluids, distributed uniformly in the turbulent channels, pipes and within the boundary layers. The heavy particles with finite St^+ , on the other hand, are less responsive to high-frequency small-scale turbulent motions, but effectively respond to eddies with similar timescales to τ_p , leading to the near-wall preferential accumulation and the clustering beneath the low-speed streaks of the fluid [15–18]. This behavior is most pronounced for particles with $St^+ = 10 \sim 100$ at low to moderate Reynolds numbers but are gradually alleviated when St^+ further increases [19–21]. At high Reynolds numbers, the emergence of large-scale and very-large-scale motions, along with the hierarchical structures in the logarithmic region, further enhances particle streaks of varying spanwise widths, depending on the consistency between τ_p and eddy turn-over time [4, 22–24].

As the mass loading φ_m surpasses a threshold higher than $O(0.1)$, the feedback force from the particle to turbulence commences to play an important role [25]. This modulation of turbulence by particles is evident flow characteristics such as mean velocity, Reynolds stress, and the morphology and intensity of the turbulent structures [7, 8]. In terms of turbulent kinetic energy transfer, Zhao *et al.* [26] demonstrated that the particle force acting on the fluid enhances the near-wall turbulence while attenuates it in the core region of the channel. They also highlighted the imbalance in work exchange between particles and the fluid due to slip velocity, leading to additional dissipation of kinetic energy known as the ‘particle dissipation’. However, this dissipation is insufficient to impede the enhancement of streamwise velocity fluctuations. Pan *et al.* [27] investigated the impact

of particles on mean and turbulent kinetic energy, concluding that particles extract energy from the mean flow and redistribute it to turbulent kinetic energy throughout the channel.

The influence of particles on turbulence depends on both the particle Stokes number St^+ and the mass loading φ_m , with the latter being more pivotal in comparison [11, 28, 29]. Zhao *et al.* [30] performed direct numerical simulation (DNS) for a turbulent channel flow laden with spherical particles with $St^+ = 30$ and mass loading of 1.0, observing drag reduction and turbulence attenuation compared to regular turbulent flows without particles. In the experimental study of Kulick *et al.* [31], it is found that particles generally attenuate turbulence, particularly affecting specific wavenumbers or scales of motion. Turbulent suppression is more pronounced in channels than in isotropic turbulence. Li *et al.* [32] demonstrated that turbulent Reynolds stress exhibits increased anisotropy as mass loading rises, attributed to modifications in the velocity-pressure gradient term, specifically the pressure-strain term in the turbulent kinetic energy (TKE) budget. As a matter of fact, all the transport terms of turbulent kinetic energy and enstrophy transport are reduced in the presence of particles [33]. Moreover, the turbulent modification is dependent on both the wall-normal location and scales. Particles tend to diminish production terms across all scales and throughout the channel, with the particle feedback effect being comparatively minor [34]. Particle clustering, dependent on the Stokes number, acts as either an energy source or sink, affecting turbulent motions at certain scales [28, 34]. By conditional averaging the flow field surrounding the streamwise vortices, Dritselis and Vlachos [35] observed that particle feedback forces generate a torque opposing the rotation of streamwise vortices, thereby reducing vorticity magnitude. In terms of flow topology, Mortimer and Fairweather [36] noted that heavy particles lower the possibility of finding particles in unstable focus/compressing regions and stable focus/stretching regions across the channel, corresponding to the streamwise vortices.

The modulation of turbulence by the Stokes number St^+ is primarily influenced by changes in preferential concentration, which impacts the spatial distribution and magnitude of the feedback force. Wu *et al.* [37] investigated the effects of St^+ at a mass loading of 0.2 and observed that turbulent production and viscous dissipation exhibit non-monotonic variations, with the most significant suppression occurring for particles with $St^+ = 40$. This suppression is achieved by accelerating the low-speed and decelerating the high-speed fluid [38]. Additionally, the size of the streamwise vortices increases with longer particle response times, while the intensities of velocity and vorticity fluctuations are diminished, yet show an increasing trend with the Stokes number [39]. Conversely, particles with $St^+ = 0.5$ enhance the instability of streaks and more effectively generate quasi-streamwise vortices [38]. Richter and Sullivan [40] found that in turbulent Couette flows, the maximum feedback force is realized at a Stokes number of $O(1)$, under the Kolmogorov scale. Wang and Richter [41] demonstrated that high-inertia particles reduce the stretching and lift-up effects in the regeneration cycle of near-wall turbulence, thereby suppressing the formation of streaks and vortices. Furthermore, the two-way coupling mechanism decreases particle velocity fluctuations and near-wall particle concentration,

with the extent of these reductions increasing with mass loading [42].

There exists a critical mass loading threshold beyond which turbulence is entirely disrupted. At low mass fractions, particles suppress vortical motions, thereby diminishing sweeping and ejection events and reducing Reynolds stresses, which are nearly offset by the momentum imparted by the particles [28]. This effect is stronger with the increasing mass fractions φ_m [43]. However, the intensity of streamwise velocity fluctuations varies non-monotonically with mass loading, first decreasing and then increasing, with the critical variation caused by the direction in which the turbulent kinetic energy is transferred [43]. Vreman [11] extensively discussed the impacts of particle mass loading, noting that at low mass loadings, the dissipation due to particle forces is minor compared to other turbulent kinetic energy transfer mechanisms. Conversely, at moderate to high mass loadings, where turbulent intensities are lower, turbulent motions are predominantly induced by particle dynamics rather than conventional turbulent mechanisms. This leads to a gradual weakening of coherent structures, accompanied by more uniform particle distributions in turbulent pipe flows, both radially and along wall-parallel planes. Muramulla *et al.* [29] further showed that the critical values for laminarization depend on the Stokes number but are less influenced by the choice of force model. Beyond this critical value, the abrupt decreasing production term, rather than the particle drag dissipation, is primarily responsible for flow relaminarization.

The aforementioned conclusions pertain solely to incompressible turbulent flows. In the realm of compressible flows, such research is relatively sparse. In compressible homogeneous isotropic turbulence, it has been observed that particles not only accumulate in regions of high shear but also behind shocklets, thereby diminishing both rotational and dilatational motions [44, 45]. Fluctuations are mitigated at low wavenumbers while being enhanced at high wavenumbers [45]. Thermodynamic flow properties are reduced, yet the mean temperature and pressure are elevated, effects that intensify with the Stokes number, attributed to increased internal energy production [46]. In compressible homogeneous shear turbulence, larger particles diminish cross-stream velocity fluctuations, curtail the growth rate of the mixing layer, and weaken both vortices and shocklets. [47–49]. Chen *et al.* [50] examined particle-laden compressible turbulent boundary layers involving combustion, finding that large and heavy particles suppress streamwise vortices, leading to a homogeneous particle distribution, yet these particles still predominantly concentrate in strain-dominant regions. The fluid temperature and wall heat flux are substantially decreased due to particle heat transfer. Additionally, studies focusing solely on the one-way coupling in particle-laden compressible wall-bounded turbulence have revealed no significant differences from incompressible wall-bounded turbulence in terms of particle statistics and preferential accumulation [13, 14, 51].

The preliminary literature review indicates that while particle-laden flows have been extensively studied in the context of incompressible wall-bounded turbulence, there is a notable gap in understanding when it comes to compressible flows. This gap serves as the motivation for the current study. In this paper, we conduct direct numerical simulations of particle-laden compressible turbulent boundary layer flows at a free-stream Mach

number of 2.0, utilizing the Eulerian-Lagrangian point-particle method. Our analysis is confined to considering the feedback force exerted by the particles on the fluid, deliberately omitting the heat transfer between them. The primary focus is on the modulation of momentum and kinetic energy transfer by the particles, the variations in turbulent statistics influenced by the particle Stokes number St^+ and mass loading, and the impact of particle feedback forces on turbulent motions across different scales. The findings presented here are intended to enhance the accuracy of modeling and predicting such flows.

The remainder of this paper is organized as follows. In section II we introduce the numerical methods adopted in conducting the two-way coupling of particle-laden compressible turbulent boundary layers and the flow parameters. In section III we discuss in detail the modulations of particles on the instantaneous flow fields, the mean velocity and Reynolds stress, momentum balance and kinetic energy transfer and the mean temperature of the fluid. The conclusions are given in section IV.

II. NUMERICAL METHOD

We consider the compressible turbulent boundary layers carrying dilute phase small spherical particles with negligible volume fraction but finite mass loading. The Eulerian-Lagrangian point-particle approach is still valid for simulating such flows. Both the forces acting on the particles and their feedback to the fluid should be considered, constituting a two-way coupling between them. The compressible turbulent boundary layer flows are governed by the three-dimensional Navier-Stokes equation for perfect Newtonian gases,

$$\frac{\partial \rho}{\partial t} + \frac{\partial(\rho u_i)}{\partial x_i} = 0, \quad (1)$$

$$\frac{\partial(\rho u_i)}{\partial t} + \frac{\partial(\rho u_i u_j)}{\partial x_j} = -\frac{\partial p}{\partial x_i} + \frac{\partial \tau_{ij}}{\partial x_j} + F_{p,i}, \quad (2)$$

$$\frac{\partial(\rho E)}{\partial t} + \frac{\partial(\rho E u_j)}{\partial x_j} = -\frac{\partial(p u_j)}{\partial x_j} + \frac{\partial(\tau_{ij} u_i)}{\partial x_j} - \frac{\partial q_j}{\partial x_j} + F_{p,i} u_i. \quad (3)$$

Here, ρ is the fluid density, and u_i ($i = 1,2,3$) is the velocity component of the fluid in the x_i direction, (also x , y and z , corresponding to the streamwise, wall-normal and spanwise directions). The p is pressure and E is total energy, following the state equations of the perfect gases

$$p = \rho R T, \quad E = C_v T + \frac{1}{2} u_i u_i, \quad (4)$$

with T being the temperature, R being the gas constant and C_v being the constant volume specific heat. The τ_{ij} is the viscous stress tensor and q_j is the molecular heat conductivity, associated with the velocity and temperature gradients as follows

$$\tau_{ij} = \mu \left(\frac{\partial u_i}{\partial x_j} + \frac{\partial u_j}{\partial x_i} \right) - \frac{2}{3} \mu \frac{\partial u_k}{\partial x_k} \delta_{ij}, \quad q_j = -\kappa \frac{\partial T}{\partial x_j} \quad (5)$$

in which μ is the fluid viscosity, determined by Sutherland's law, and $\kappa = C_p\mu/Pr$ is the molecular heat conductivity, with C_p the constant pressure specific heat and $Pr = 0.71$ the molecular Prandtl number. $F_{p,i}$ is the feedback force from the particles to the fluid, which will be introduced subsequently.

The boundary conditions are specified as follows. At the lower wall, no-slip and no-penetration conditions are given for velocity and the isothermal condition is given for temperature. The outflow and no-reflecting conditions are adopted at the upper and streamwise outlet boundaries. The periodic conditions are used in the spanwise direction. The turbulent inflow is given at the inlet boundary, composed of the mean velocity profiles given according to the empirical formula by Musker [52], the mean temperature profiles obtained by the generalized Reynolds analogy [53], and the velocity and temperature fluctuations by digital filtering method [54].

The governing equations are solved directly by the finite difference method using the open-source code developed by Bernardini *et al.* [55]. The convective terms are approximated by the sixth-order kinetic energy preserving scheme [56] and the viscous terms are expanded into Laplacian forms and approximated by the sixth-order central scheme [57]. Time advancement is achieved by the third-order low-storage Runge-Kutta scheme [58].

The motions of the particles are solved by the following equations

$$\frac{dr_{p,i}}{dt} = v_i, \quad \frac{dv_i}{dt} = \frac{f_D}{\tau_p}(u_i - v_i). \quad (6)$$

Here, $r_{p,i}$ and v_i are the position and velocity of the particles, and τ_p is the particle relaxation time, defined as $\tau_p = \rho_p d_p^2 / (18\mu)$, with ρ_p the particle density and d_p the particle diameter. The coefficient f_D incorporates variation of the drag force with the particle Reynolds number $Re_p = \rho|u_i - v_i|d_p/\mu$ and the particle Mach number $M_p = |u_i - v_i|/\sqrt{\gamma RT}$ following the suggestion of Loth *et al.* [10] writes as

$$f_D = (1 + 0.15Re_p^{0.687})H_M, \quad (7)$$

$$H_M = \begin{cases} 0.0239M_p^3 + 0.212M_p^2 - 0.074M_p + 1, & M_p \leq 1 \\ 0.93 + \frac{1}{3.5 + M_p^5}, & M_p > 1 \end{cases} \quad (8)$$

In our previous study regarding the one-way coupling between the fluid and particles [51], we have demonstrated that both the particle Knudsen numbers and particle Reynolds numbers are low, so the terms associated with the rarefaction effects and high Reynolds number effects that incorporate fully turbulent wakes can be neglected. The time advancement in numerically solving the position and velocity of the particles is achieved using the same third-order Runge-Kutta scheme as the fluid flow. The information of the fluid at the positions of the particles is obtained using trilinear interpolation, which has been proven to be sufficiently accurate in direct numerical simulations [13, 20]. The spanwise periodic condition is also adopted for particles. When the particles go through the streamwise outlet and upper boundaries, they are recycled to the turbulent inlet at a random position within the boundary layer thickness.

The feedback force is obtained using the particle-in-cell (PIC) approximation [26, 35], summing the forces of the particles within a mesh cell

$$F_{p,i} = -\frac{m_p}{V_{cell}} \sum_{l=1}^{n_p} \frac{f_D}{\tau_p} (u_i - v_i) \quad (9)$$

with m_p the mass of the particle, then interpolating onto the grid points using the trilinear interpolation. The heat transfer between the particles and fluid is neglected here. In other words, the particles are considered to be in a thermal equilibrium state, changing their temperature instantaneously with the ambient fluid. The effects of the particles absorbing and releasing heat from and to the fluid will be considered in our future work. The DNS solver is validated by comparing the statistics of a two-way coupling turbulent channel flow simulations at low Mach numbers with those of incompressible flows, which is given in Appendix A.

Other notations are listed as follows. The subscript 0 refers to the flow quantities in the free-stream and w to those at the wall. The ensemble average of a flow quantity ϕ is represented by $\bar{\phi}$ and the corresponding fluctuations as ϕ' . The density-weighted average is denoted by $\tilde{\phi}$ and the corresponding fluctuations as ϕ'' . The superscript + represents the normalization by the viscous scales, defined by the wall shear stress $\tau_w = (\mu_w \partial \bar{u} / \partial y)|_w$, wall mean density $\bar{\rho}_w$ and viscosity μ_w , which further gives the friction velocity $u_\tau = \sqrt{\tau_w / \bar{\rho}_w}$, the friction length scale $\delta_\nu = \mu_w / (\bar{\rho}_w u_\tau)$ and the friction Reynolds number $Re_\tau = \bar{\rho}_w u_\tau \delta / \mu_w$, with δ the boundary layer thickness.

We consider the compressible turbulent boundary layers at the free-stream Mach number $M_0 = U_0/a_0 = 2.0$ and the free-stream Reynolds number $Re_0 = \rho_0 U_0 \delta_0 / \mu_0 = 9919$, with a_0 the free-stream sound speed and δ_0 the nominal boundary layer thickness at the turbulent inlet. The wall temperature T_w is set as the recovery temperature $T_r = 1.72T_0$, defined as $T_r = T_0(1 + (\gamma - 1)Pr^{1/2}M_0^2/2)$. Correspondingly, the friction Reynolds number $Re_{\tau,0}$ at the turbulent inlet is 200. The sizes of the computational domain in the streamwise, wall-normal and spanwise directions are $L_x = 80\delta_0$, $L_y = 9\delta_0$ and $L_z = 8\delta_0$, discretized by 2400, 280 and 280 grids, respectively, with the mesh sizes of $\Delta x^+ \approx 6.67$, $\Delta y_w^+ = 0.5$ and $\Delta z^+ \approx 5.71$ under viscous scales at the turbulent inlet. According to a preliminary examination of the spatial development features, we found that the turbulence is statistically equilibrium downstream of $x = 50\delta_0$ after the simulations have been run for $1000\delta_0/U_0$. Henceforth, the turbulent statistics are given within the streamwise range $x = (60 \sim 70)\delta_0$ and a time period of $200\delta_0/U_0$.

The particle parameters are listed in Table I. We consider a one-way coupling case P0-F00 without feedback force from the particle to the fluid, and six two-way coupling cases with different particle populations and mass loadings. The particle density is set to be identical as $\rho_p = 8000\rho_0$ and the particle diameters as $d_p = 0.002\delta_0$, $0.003\delta_0$ and $0.004\delta_0$, hereinafter referred to as particle populations P1, P2 and P3, respectively. The particle Stokes numbers under viscous scales $St^+ = \tau_p u_\tau / \delta_\nu$ are different, due to the disparity in their diameters. For particle P1, the number of particles N_p in case P1-F02 is set to be 6,000,000, resulting in the mass loading, hereinafter defined as $\varphi_m = m_p N_p / (\rho_0 L_x L_z \delta)$

TABLE I. Computational parameters. Here, η_w is the Kolmogorov length scale at the wall, N_p is the particle number and φ_m is the particle mass loading.

Case	Re_τ	ρ_p/ρ_0	d_p/δ_0	d_p/η_w	St^+	N_p	φ_m	Line type
P0-F00	353	8000	0.0025	0.318	162	1,000,000	-	————
P1-F02	338	8000	0.002	0.208	103	6,000,000	0.17	-----
P1-F06	296	8000	0.002	0.214	79	20,000,000	0.57	---◆---
P2-F02	358	8000	0.003	0.351	230	1,800,000	0.17	-·-·-·-
P2-F06	337	8000	0.003	0.280	225	6,000,000	0.57	-·-■-·-
P3-F02	356	8000	0.004	0.476	410	750,000	0.17	-·-·-·-
P3-F14	301	8000	0.004	0.276	349	6,000,000	1.36	-·-▶-·-

(δ the boundary layer thickness within $x = (60 \sim 80)\delta_0$), being approximately 0.17. To retain the mass loading φ_m , we adjust the particle number for populations P2 and P3 in cases P2-F02 and P3-F02. We also design two simulations with the same particle numbers N_p as in case P1-F02, thus giving higher mass loading of $\varphi_m = 0.57$ for case P2-F06 and $\varphi_m = 1.36$ for case P3-F14, and another case P1-F06 to compare with case P2-F06 for the Stokes number effects. As reported in Table I, the friction Reynolds numbers Re_τ are only slightly modified, except for case P3-F14 where it is reduced by approximately 15%.

III. RESULTS AND DISCUSSION

A. Instantaneous distributions

In figure 1 we present the instantaneous distributions of the streamwise velocity fluctuations in the wall-parallel plane in the buffer region at $y^+ = 8$ and particles within the wall-normal range of $y^+ = 3 \sim 15$ for cases P0-F00, P1-F06, P2-F06 and P3-F14. In the one-way coupling case P0-F00, the negative regions of the velocity fluctuations are organized as the streamwise elongated streaky structures, namely the low-speed streaks, whereas the high-speed regions are comparatively shorter in the streamwise direction and wider in the spanwise direction. The particles clustered within the low-speed regions manifest similar streaky structures as the velocity, forming the streamwise-elongated structures [16]. In such regions, the particles are mostly being decelerated. In the high-speed regions, on the other hand, the particles are more frequently accelerated. Similar phenomena can be observed in cases P1-F02, P2-F02 and P3-F02 (not shown here for brevity), except for the different particle numbers near the wall due to the disparity in the particle Stokes number. In cases P1-F06 and P2-F06 with a moderate mass loading, the velocity fluctuations are slightly weakened. In these cases, the accelerated particles and decelerated particles tend to be mixing, showing less tendency to congregate within the low- and high-speed regions respectively [11, 42]. This is consistent with the findings of the previous studies that the near-wall accumulation is weakened for higher St^+ particles [38]. In case P3-F14 with the highest mass loading, the flow is almost completely laminarized, dis-

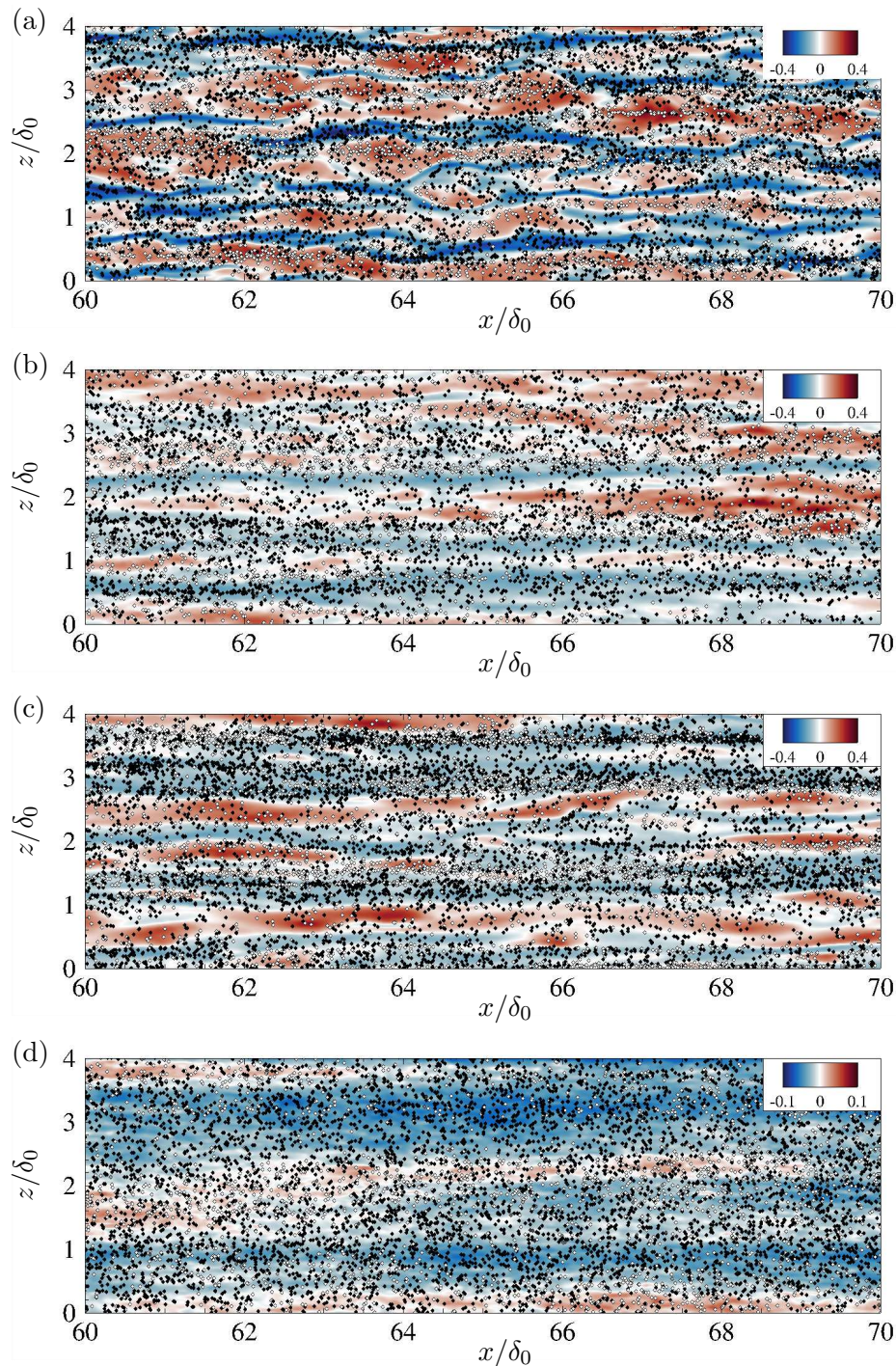


FIG. 1. Instantaneous distributions of velocity fluctuations at $y^+ = 8$ and particles within $y^+ = 3 \sim 15$, (a) case P0-F00, (b) case P1-F06, (c) case P2-F06, (d) case P3-F14. White particles: $a_1 > 0$, black particles: $a_1 < 0$.

playing only very weak velocity fluctuations. The corresponding flow structures are wider and less meandering. It seems that the near-wall velocity fluctuations are induced by the particles swept towards and reflected from the wall, instead of retaining their near-wall self-sustaining cycles in canonical wall-bounded turbulence, as pointed out by Vreman [11]. This will be further demonstrated in the subsequent discussions.

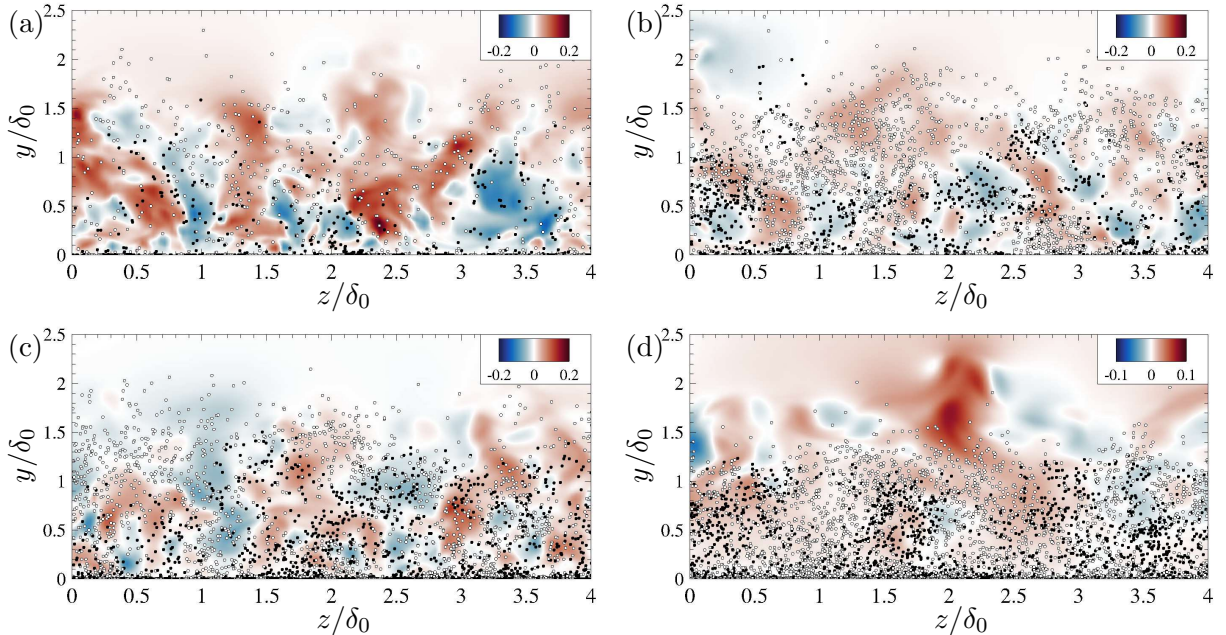


FIG. 2. Instantaneous distributions of velocity fluctuations u''_1/U_∞ in the cross-stream plane $x = 60\delta_0$ and particles within $x = (60 \sim 60.02)\delta_0$, (a) case P0-F00, (b) case P1-F06, (c) case P2-F06, (d) case P3-F14. White particles: $v_2 > 0$, black particles: $v_2 < 0$.

The cross-stream distributions of the wall-normal velocity of fluid and particles are shown in figure 2. The vertical motions of the particles are in general agreement with the trend of their streamwise accelerations, in that they are accelerated when moving away from the wall ($v_2 > 0$) and decelerated when moving towards the wall ($v_2 < 0$). In the one-way coupling case P0-F00, the particles are accumulating close to the wall, leaving only a small fraction in the outer region, where the ascending and descending particles are located almost within the ejections and sweeping regions, respectively. In cases P1-F06 and P2-F06, the degrees of the near-wall accumulation are mitigated, and the particles show a higher probability of moving in the opposite direction of the vertical motions from the fluid. The near-wall velocity fluctuation intensities are weaker, but not completely interrupted by the presence of particles. In case P3-F14, however, the particles are almost evenly distributed within the boundary layer. The wall-normal velocity fluctuations almost disappear below $y = 0.3\delta_0$, only showing comparatively intense fluctuations near the outer edge of the boundary layer, resembling the features of the turbulent mixing layers.

The observations of the instantaneous fields seem to indicate that the turbulent dynamics are strongly modulated by the particles, especially for the high mass loading case P3-F14. In the following discussions, we will present in detail the variation of flow statistics related to momentum and kinetic energy transport.

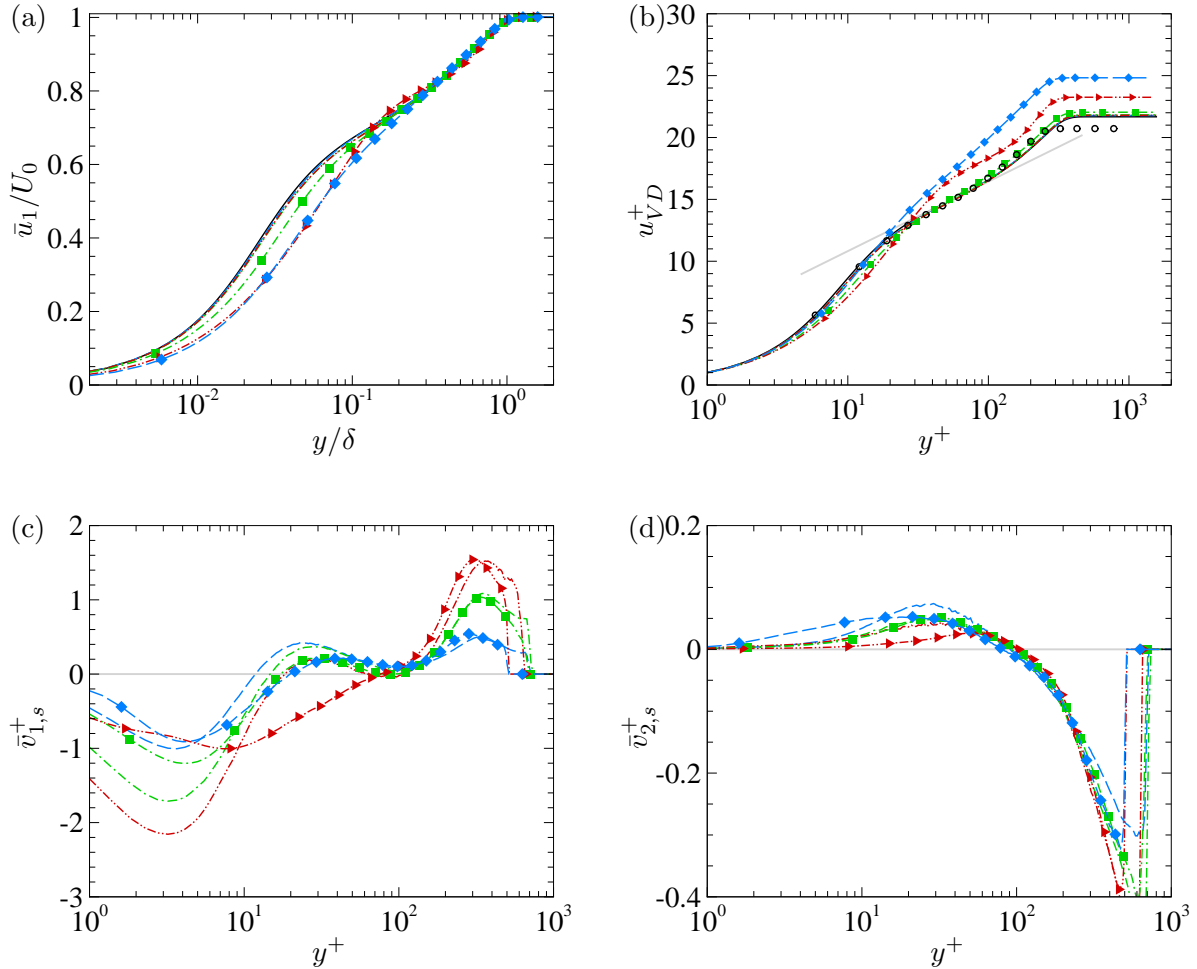


FIG. 3. Wall-normal distributions of (a) mean velocity \bar{u}_1/U_0 against y/δ , (b) van Driest transformed mean velocity u_{VD}^+ , (c) streamwise mean slip velocity $\bar{v}_{1,s}/U_0$ and (d) wall-normal mean slip velocity $\bar{v}_{2,s}/U_0$. Line legends refer to Table I. Black circles: data reported by Pirozzoli and Bernardini [59] at $M_0 = 2$ and $Re_\tau = 250$.

B. Velocity statistics and mean momentum balance

In figure 3(a,b) we present the wall-normal distributions of the mean velocity in outer scales and under van Driest transformation

$$u_{VD}^+ = \int_0^{\bar{u}^+} \sqrt{\frac{\bar{\rho}}{\bar{\rho}_w}} d\bar{u}, \quad (10)$$

along with the data reported by Pirozzoli and Bernardini [59] at $M_0 = 2$ and $Re_\tau \approx 250$. Compared with the one-way coupling case P0-F00, the mean fluid velocity in cases P1-F02, P2-F02 and P3-F01 with low mass loadings are not much affected, suggesting the weak influences of the particles in these cases. For higher mass loadings cases P1-F06, P2-F06 and P3-F14, on the other hand, the mean velocities are significantly lower in the near-wall region but higher in the outer region, corresponding to the reduction of the skin friction. The particle population P1 with $St^+ \approx 100$ with the highest degree of near-

wall preferential accumulation seems to leave the strongest impact, even though the mass loading in case P1-F06 is less a half of that in case P3-F14. Similar phenomena have been found in the previous studies of turbulent flows [29, 36, 38, 40], in which it is pointed out that both the Stokes number and the mass loadings are responsible for turbulent modulation. Despite the similarity of the near-wall mean velocity in cases P1-F06 and P3-F14, the origin of turbulent motions, as we will demonstrate later, are completely different.

Due to the finite inertia of the particles, the mean particle velocities are different from those of the fluid. This can be evaluated by the mean slip velocity in the average sense, as shown in figures 3(c,d). It is defined as $\bar{v}_{i,s} = \bar{u}_{i,p} - \bar{v}_i$, where $u_{i,p}$ is the fluid velocity at the particle positions. The streamwise component $\bar{v}_{1,s}$ is negative below $y^+ \approx 10$ and positive above that location for cases with low and moderate mass loadings, while the negative region extends to $y^+ \approx 80$ for case P3-F14 with the highest mass loading. This suggests that the particles are moving faster than the fluid in the near-wall region but slower in the outer region in the average sense. The wider extent of the negative $\bar{v}_{1,s}$ in case P3-F14 can be attributed to the less effective deceleration effects in the comparatively quiescent flows, considering their laminarization in the near-wall region. From another perspective, the negative slip velocity $\bar{v}_{1,s}$ also implies that the fluid is being accelerated in the near-wall region, introducing extra shear rates. This explains why the skin frictions are only reduced slightly when the near-wall turbulence is much weakened. The wall-normal slip velocities $\bar{v}_{2,s}$ are positive below $y^+ \approx 100$. It can be inferred that the particles are more inclined to congregate within the ejection regions, the tendency of which is alleviated by the higher Stokes number St^+ and mass loading φ_m .

The mean velocity distribution both depends on and determines the mean streamwise momentum transport. Under the conditions of the temporally statistically steady, the streamwise mean momentum equation can be formulated as

$$\frac{\partial \bar{\tau}_{12}}{\partial y} - \frac{\partial \overline{\rho u_1'' u_1''}}{\partial y} + \bar{F}_{p,1} = \frac{\partial \bar{\rho} \tilde{u}_1 \tilde{u}_1}{\partial x} + \frac{\partial \bar{\rho} \tilde{u}_1 \tilde{u}_1}{\partial y} - \frac{\partial \bar{\tau}_{11}}{\partial x} + \frac{\partial \overline{\rho u_1'' u_1''}}{\partial x}, \quad (11)$$

with the right-hand-side representing the spatial development and mean flow convection. Integrating this formula in the wall-normal direction, the left-hand-side terms can be cast as

$$\tau_v = \tau_{12} = \bar{\mu} \left(\frac{\partial \bar{u}_1}{\partial y} + \frac{\partial \bar{u}_2}{\partial x} \right), \quad \tau_r = -\overline{\rho u_1'' u_2''}, \quad \tau_p = \int_y^\delta F_{p,1} dy \quad (12)$$

namely the viscous shear stress, the Reynolds shear stress and the particle shear stress. Note that the integration is performed from the outer edge of the boundary layer to the wall to avoid non-zero τ_p in the free-stream, which is misleading and unphysical. Their summation is referred to as the total shear stress

$$\tau_t = \tau_v + \tau_r + \tau_p. \quad (13)$$

It should be equivalent to the integration of the streamwise development terms on the right-hand-side of Equation (11) but in the opposite sign.

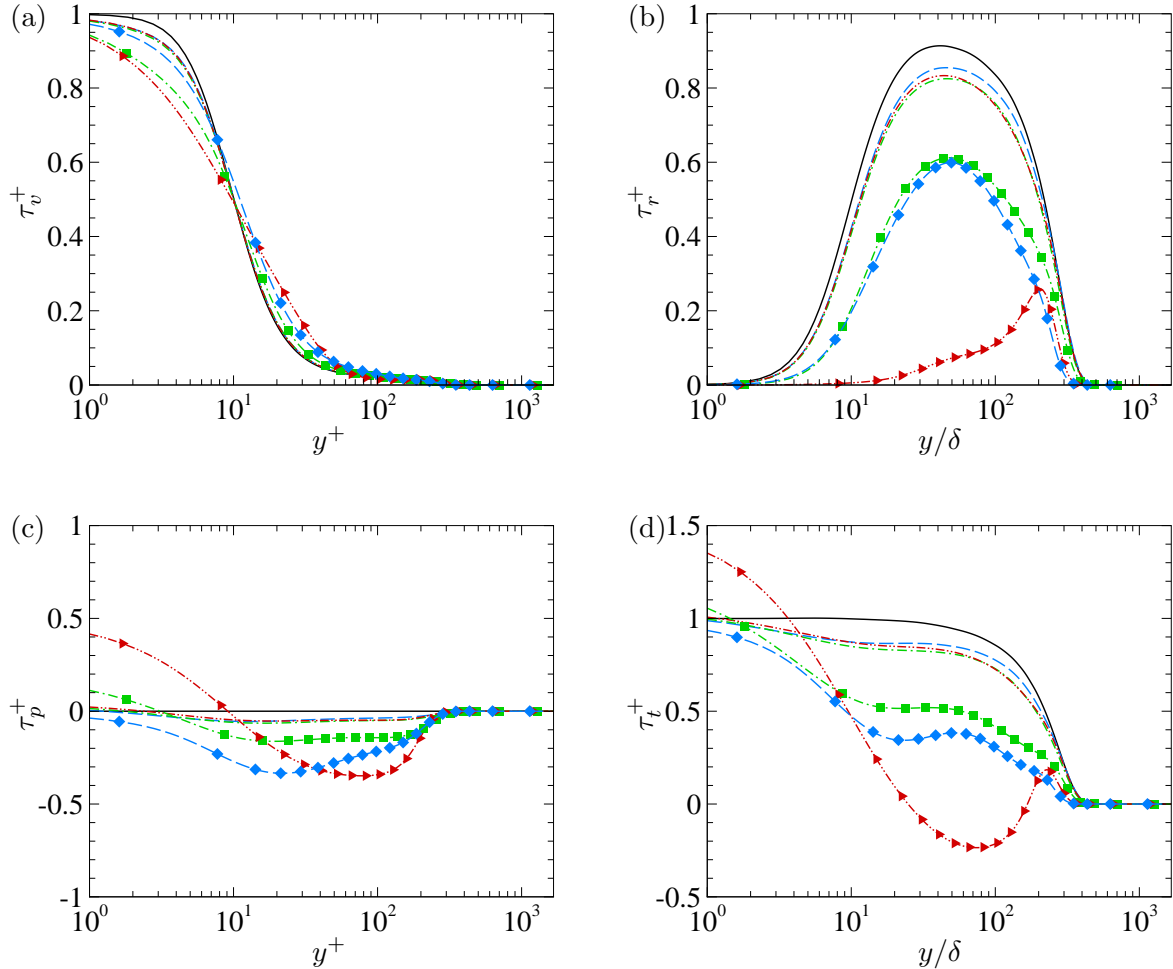


FIG. 4. Wall-normal distribution of (a) viscous shear stress τ_v , (b) Reynolds shear stress τ_r , (c) particle force τ_p and (d) total stress τ_t . Line legends refer to Table I.

Figure 4 shows the wall-normal distribution of the shear stresses given above. Consistent with the previous observations in the mean velocity, these shear stresses are only weakly affected in low mass loading cases P1-F02, P2-F02 and P3-F02, but are strongly modulated in the rest of the cases, the degree of which is dependent on both the mass loadings φ_m and the particle Stokes number St^+ . As the φ_m increases, the τ_v is decreased below $y^+ \approx 10$ but is increased above it. The τ_t is decreased monotonically with the φ_m . In cases P1-F06 and P2-F06, the peaks in the near-wall region still exist but are significantly lower, suggesting that the turbulent motions are only disturbed to be weakened in these cases. In case P3-F14, however, the near-wall peak completely disappears, leaving only comparatively high values near the edge of the boundary layer, in agreement with our observations from the instantaneous flow fields that the turbulence is only active in the outer region for case P3-F14. This also supports our previous statement that the near-wall turbulent motions are completely different in cases P1-F06 and P3-F14, despite the similarity in the mean velocity profiles. The particle shear stress τ_p constitutes less than 10% for cases with $\varphi_m = 0.17$, but finitely by approximately -10% in case P2-F06

and -30% in case P1-F06 in the buffer layer and P3-F14 in the logarithmic layer, respectively. Moreover, in case P3-F14, this term constitutes approximately 40% in the viscous sublayer. The important role played by particles in case P1-F06 can be attributed to the effective response of particles to the fluid motions, and that in case P3-F14 merely to the high mass loading. Further increasing the mass loading for particle populations P1 and P2 will probably give the same results, but the critical value of φ_m resulting in the flow laminarization depends on the particle Stokes number, as pointed out by Muramulla *et al.* [29]. Correspondingly, the summation of these terms, i.e. the total shear stress τ_t is merely slightly reduced in cases P1-F02, P2-F02 and P3-F02, but highly affected in the other three cases with moderate and high mass loadings, showing non-monotonic trend of variation along the wall-normal direction. Considering such significant variations, it is probably necessary to reconsider the strategy of turbulent modelling and predictions in particle-laden flows.

C. Skin friction and its decomposition

The alteration of the momentum balance will further result in the variation of skin friction. In figure 6 we present the distributions of the skin friction C_f against the incompressible counterpart of the momentum Reynolds number Re_{δ_2} , defined as

$$Re_{\delta_2} = Re_{\theta_i} = \frac{\rho_0 U_0 \theta}{\mu_w}, \quad \theta = \int_0^\delta \frac{\bar{\rho} \bar{u}}{\rho_0 U_0} \left(1 - \frac{\bar{u}}{U_0}\right) dy. \quad (14)$$

It has been shown by Hopkins and Inouye [60] that the friction law for the incompressible turbulent boundary layers $C_{f,i} = 0.024 Re_{\theta_i}^{-1/4}$ can be applied to the compressible turbulence over adiabatic walls if the following factors are incorporated

$$C_{f,i} = F_c C_f, \quad F_c = \frac{T_w/T_0 - 1}{\arcsin^2 \alpha}, \quad \alpha = \frac{T_w/T_0 - 1}{\sqrt{T_w/T_0(T_w/T_0 - 1)}}. \quad (15)$$

For the one-way coupling case P0-F00, the skin friction C_f obeys the friction law after a streamwise extent of flow adjustment towards the equilibrium state. For cases P1-F02, P2-F02 and P3-F02, the skin frictions are slightly reduced compared with the case P0-F00, and the influences of the particle Stokes numbers are weak. In cases with low and moderate mass loadings (P1-F06, P2-F06 and P3-F14), the skin frictions firstly overshoot to higher values, then decrease rapidly downstream, violating their power-law correlations with Re_{θ_i} in compressible turbulent boundary layers. Consistent with the previous observations, the skin friction in case P1-F06 is the most affected, reduced by approximately 30% compared with the one-way coupling case, even lower than case P2-F06 with the same mass loading, suggesting that the evident particle preferential accumulation in this case modulates the near-wall turbulence significantly. This is reasonable, for in a low Reynolds number turbulence where no large-scale and very-large-scale motions can be found, near-wall turbulence is, perhaps, the most crucial, the intrusion or disruption of which thus reduces the skin friction most effectively.

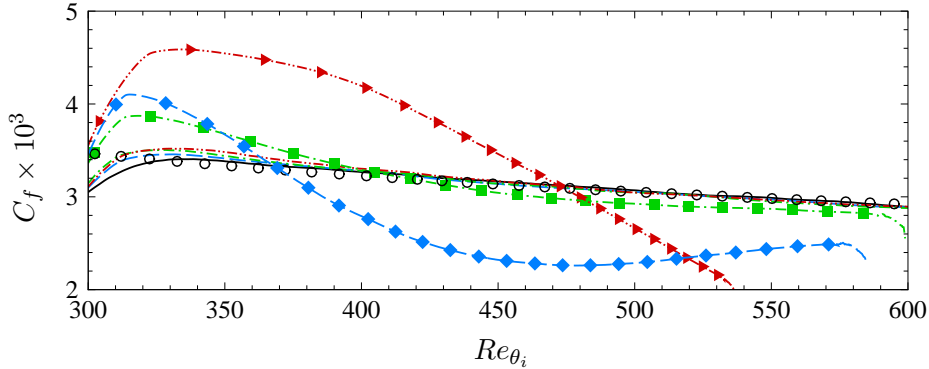


FIG. 5. Variation of the skin friction C_f with Re_{θ_i} . Line legends refer to Table I. Symbols: turbulent friction law $C_{f,i}/F_c$.

TABLE II. Contribution of C_V , C_R , C_G and C_P to the skin friction at $Re_{\theta_i} = 450$.

Case	C_V/C_f	C_R/C_f	C_G/C_f	C_P/C_f
P0-F00	9.97%	70.10%	19.93%	0.00%
P1-F02	10.05%	49.73%	33.87%	6.35%
P1-F06	13.40%	38.67%	23.59%	24.38%
P2-F02	10.13%	47.49%	34.57%	7.81%
P2-F06	10.55%	31.74%	26.62%	31.09%
P3-F02	10.05%	47.50%	34.79%	7.66%
P3-F14	9.87%	8.87%	13.26%	68.00%

To further explore the influences of the particle feedback forces and the other momentum balance terms on the variation of the skin friction, we decompose the skin friction using the formula below, which is obtained by the two-fold integration of the mean momentum equation following [61],

$$C_f = \underbrace{\frac{2}{\rho_0 U_0^2 \delta} \int_0^\delta \tau_{12} dy}_{C_V} - \underbrace{\frac{2}{\rho_0 U_0^2 \delta} \int_0^\delta \overline{\rho u_1'' u_2''} dy}_{C_R} + \underbrace{\frac{2}{\rho_0 U_0^2 \delta} \int_0^\delta (y - \delta) \bar{F}_{p,1} dy}_{C_P} + \underbrace{\frac{2}{\rho_0 U_0^2 \delta} \int_0^\delta (y - \delta) I_x dy}_{C_G} \quad (16)$$

with I_x expressed as

$$I_x = -\frac{\partial \bar{\rho} \tilde{u}_1 \tilde{u}_1}{\partial x} - \frac{\partial \overline{\rho u_1'' u_1''}}{\partial x} - \frac{\partial \bar{\rho} \tilde{u}_1 \tilde{u}_2}{\partial y} - \frac{\partial \bar{p}}{\partial x} + \frac{\partial \bar{\tau}_{11}}{\partial x}. \quad (17)$$

The terms C_V , C_R , C_P and C_G on the right-hand-side of equation (16) originate from the integration of the viscous shear stress, Reynolds shear stress, particle feedback force and the mean flow convection.

The results are reported in figure 6, and their respective contributions to the total skin friction at $Re_{\theta_i} = 450$ are listed in Table II. For the one-way coupling case P0-F00, the contribution of each term to the skin friction is consistent with that reported in previous studies in canonical turbulent boundary layers [61], in that the viscous shear stress C_V

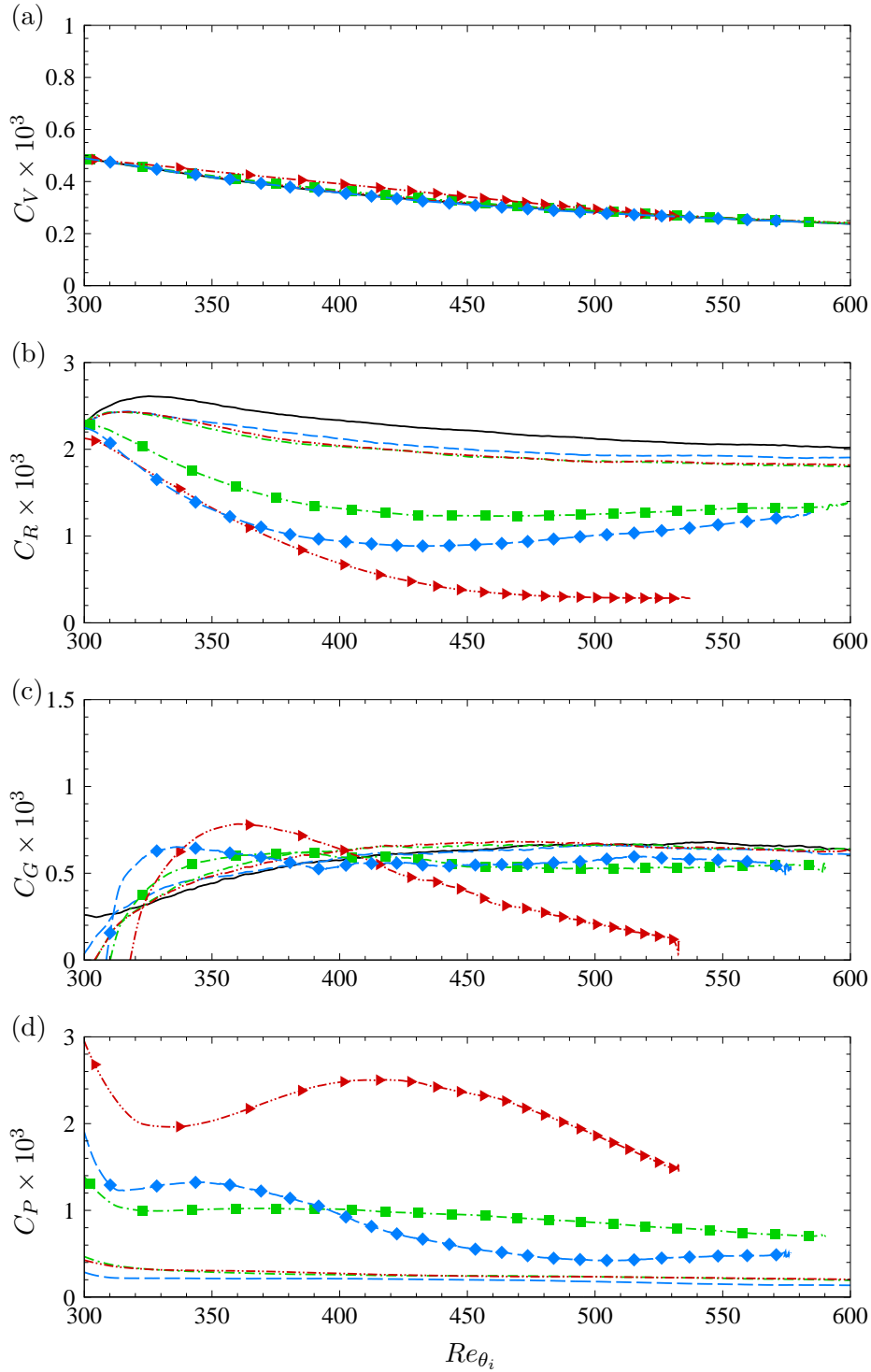


FIG. 6. Skin friction decomposition, (a) C_V , (b) C_R , (c) C_G and (d) C_P . Line legends refer to Table I.

contribute by approximately 10%, the Reynolds shear stress C_R by approximately 70%, and the mean flow convection C_G by approximately 20%. In the two-way coupling cases, the contributions of the viscous shear stress C_V remain almost unchanged for all the cases considered. The contribution from the Reynolds shear stress C_R decreases due to the lower intensity of the near-wall turbulence, the trend of which is identical to those given

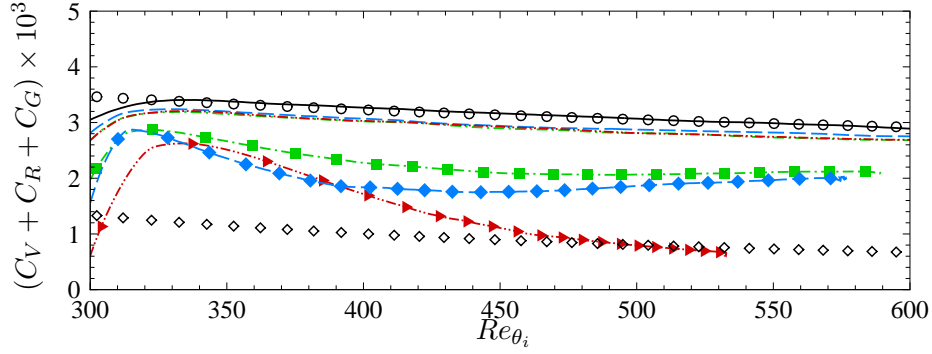


FIG. 7. Variation of $C_V + C_R + C_G$ with Re_{θ_i} , line legends refer to Table I, circles: turbulent friction law, diamonds: laminar friction law.

in figure 4(b). The mean flow convection term C_G is not much affected in low and moderate mass loading cases, manifesting the trend of converging to a constant value at $Re_{\theta_i} > 450$, while for high mass loading case P3-F14, this term decreases monotonically with Re_{θ_i} , suggesting that the particles are inhibiting the spatial development of the boundary layer. The particle feedback force term increases with the mass loading. Its contribution to case P3-F14 is the highest, but varies non-monotonically with Re_{θ_i} , increasing to reach a peak value first then decreasing rapidly. This term is much higher than the other components, contributing approximately 68% to the skin friction at $Re_{\theta_i} = 450$. In the other cases, however, its contribution remains almost a constant value at $Re_{\theta_i} > 450$, being approximately 7% in cases with $\varphi_m = 0.17$, 24% in case P1-F06 and 31% in case P2-F06.

Adding the C_V , C_R and C_G terms that are irrelevant to the particle feedback forces, as shown in figure 7, we found that the result of case P3-F14, in which the near-wall flow is laminarized, gradually falls to the friction law of laminar boundary layers $C_{f,i} = 0.44/Re_{\theta_i}$. This is interesting and probably useful for probing the skin friction laws for particulate flows, especially those with high mass loadings where the near-wall turbulence is suppressed, but more numerical simulations will be needed to achieve this task.

D. Kinetic energy transport

In this subsection, we discuss the mean and turbulent kinetic energy and their transport subject to the influences of the feedback forces from the particles.

The density-weighted velocity fluctuation intensities, evaluated by the square root of the Reynolds normal stresses, are shown in figure 8, along with the Reynolds shear stress. The pre-multiplied spanwise spectra that reflect the scale-by-scale kinetic energy are displayed in figure 9. For cases P1-F02, P2-F02 and P3-F02 with low mass loadings, the near-wall high turbulent intensities persist, but the magnitudes are lower and the spanwise characteristic length scales are slightly wider, consistent with our previous observations in the instantaneous near-wall turbulence and the results in incompressible

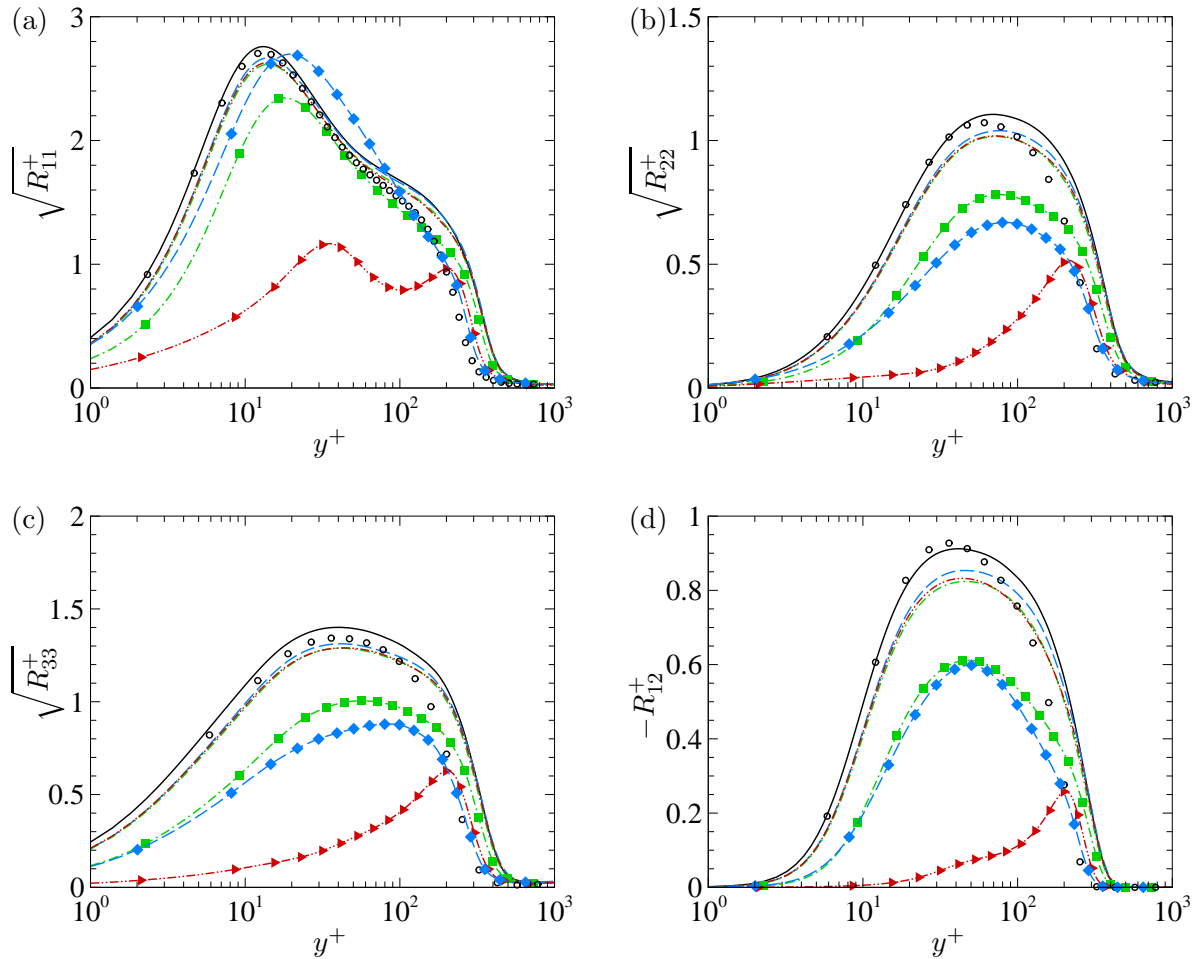


FIG. 8. Distributions of (a) $\sqrt{R_{11}^+}$, (b) $\sqrt{R_{22}^+}$, (c) $\sqrt{R_{33}^+}$, (d) Reynolds shear stress $-R_{12}^+$. Line legends refer to Table I. Black circles: data reported by Pirozzoli and Bernardini [59] at $M_0 = 2$ and $Re_\tau = 250$.

wall-bounded turbulence [28, 38, 43]. In cases with moderate mass loadings, the wall-normal and spanwise velocity fluctuation intensities are further decreased, with those in case P1-F06 slightly lower than those in case P2-F06. The streamwise velocity fluctuation intensities are increased in the former, thus resulting in stronger anisotropy, but this trend is reversed in the latter. From the turbulent kinetic energy spectra, we found that the peaks are reached at larger spanwise widths and higher wall-normal locations, with the spectra intensity stronger in case P1-F06. Both the phenomena above indicate that the particle population P2 suppresses the near-wall turbulence at all scales, but the population P1 suppresses the turbulent motions at the scale of $\lambda_z^+ = 100$ but enhances those at the scale of $\lambda_z^+ = 200$. Such a scale-dependent turbulence modulation will be discussed subsequently by showing the work of the particle feedback force. In case P3-F14, the wall-normal and spanwise velocity fluctuation intensities and the Reynolds shear stress are highly reduced below $y^+ \approx 200$. The near-wall peaks completely disappear, only showing high intensities above $y^+ \approx 100$. This conforms to the features of the turbulent fluctuations reflected by the flow structures as presented in figure 2. The streamwise

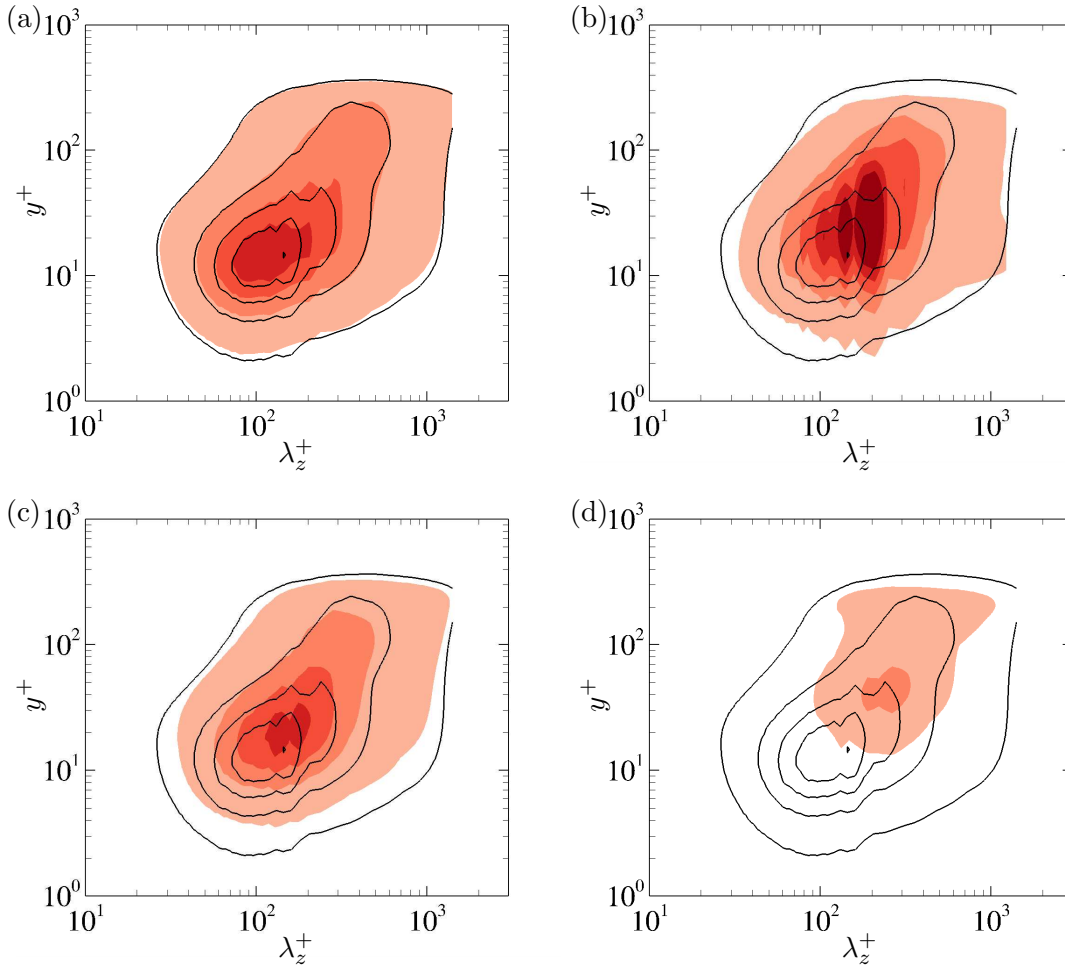


FIG. 9. Pre-multiplied spanwise spectra of turbulent kinetic energy, lines: case P0-F00, flooded: (a) P1-F02, (b) P1-F06, (c) P2-F06, (d) P3-F14. Contour levels: (0.2, 0.8, 1.4, 2.0, 2.6).

velocity fluctuation intensity in this high mass loading case manifests a near-wall peak at $y^+ \approx 40$ with the spanwise characteristic scale of $\lambda_z^+ \approx 200$. This intense near-wall peak is different from the rest of the Reynolds stress components. Since the sweeping and ejections and the streak meandering are absent in the inner region, such a high intensity can only be attributed to the particle feedback force, as can be envisaged as follows. The feedback force is expected to be positive, generated in the process of the particle sweeping towards the wall and decelerating, thereby leading to the acceleration of the fluid. Due to their high inertia, the particles are decelerated tardily, hitting and bouncing off the wall before they follow the trace of quiescent fluid motions and, at least a part of them, reentry into the active turbulent regions [11].

We further examine the turbulent kinetic energy transport and the roles played by the particle forces. The turbulent kinetic energy transport equations can be cast as

$$\frac{\partial K_t}{\partial t} + \frac{\partial \bar{u}_j K_t}{\partial x_j} = \underbrace{-\overline{\rho u_i'' u_j''}}_{P_K} \frac{\partial \tilde{u}_i}{\partial x_j} + \underbrace{\frac{\partial}{\partial x_j} (-\overline{\rho u_k'' u_k'' u_j''} - \overline{p' u_j''} + \overline{\tau_{ij}' u_i''})}_{D_K} + \underbrace{\overline{\tau_{ij}' \frac{\partial u_i'}{\partial x_j}}}_{\varepsilon_K} + \overline{F_{p,i}' u_i''} \quad (18)$$

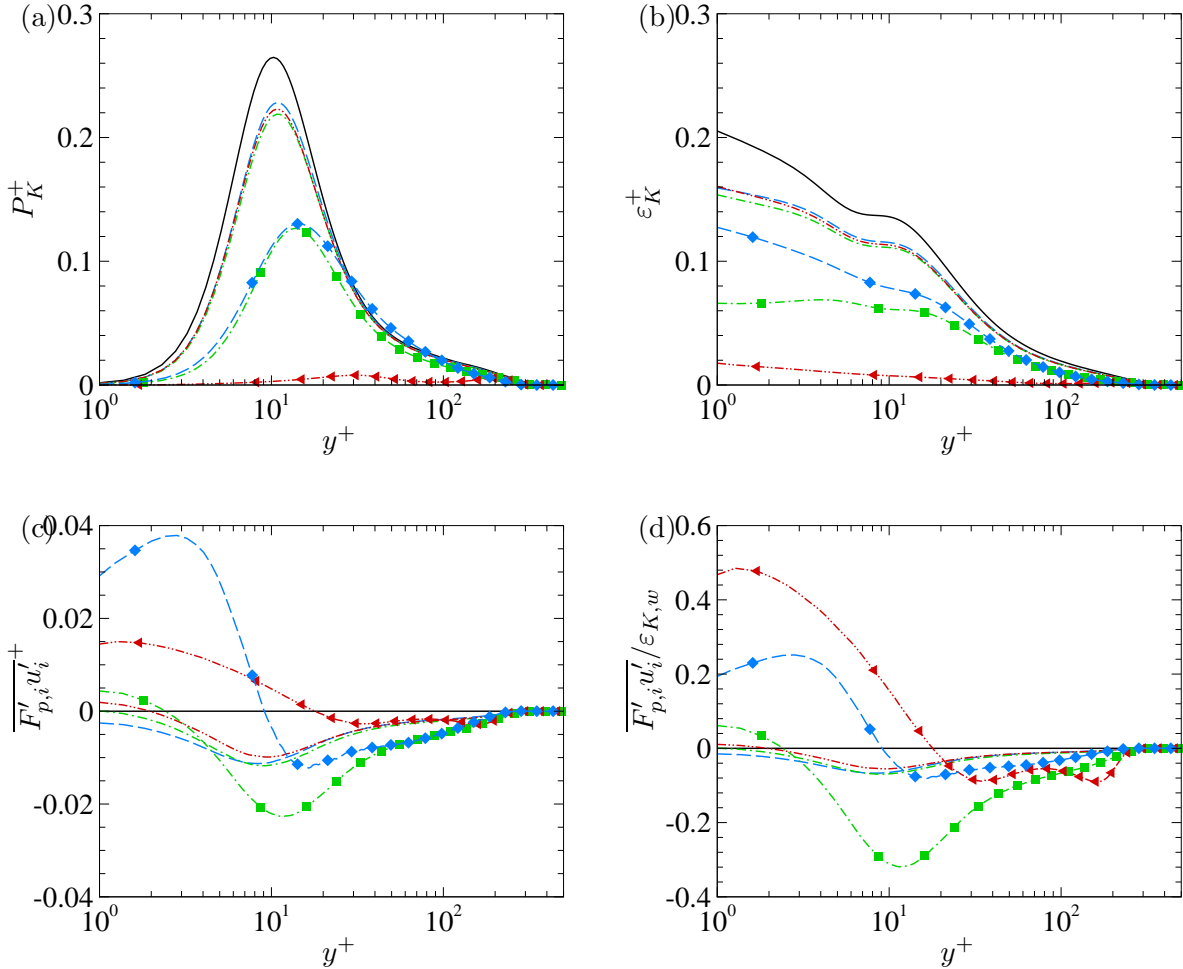


FIG. 10. Wall-normal distribution of (a) TKE production P_K^+ , (b) TKE dissipation ϵ_t^+ , (c) TKE production by particle force $\overline{F'_{p,i}u'_i}^+$ and (d) $\overline{F'_{p,i}u'_i}/\epsilon_{K,w}$ normalized by TKE dissipation on the wall. Line legends refer to Table I.

where the right-hand-side corresponds to the turbulent kinetic energy production by the mean shear, spatial diffusions, viscous dissipation and the work by fluctuating particle forces. In the following discussions, we neglect the convective terms and the spatial diffusion terms, for these terms do not generate energy in the integral sense.

In figure 10(a) we present the production term that extracts energy from the mean flow to turbulence. Although neither the mean flow nor the Reynolds stresses are much affected by the low mass loading, the production term is reduced by approximately 15% compared with the one-way coupling case. In cases P1-F06 and P2-F06, the production term is further reduced, but the near-wall peaks still exist. In case P3-F14 with the high mass loading, the production term almost falls to zero, especially in the near-wall region, further proving our inference that the near-wall high turbulent intensities are not generated by turbulent motions of the fluid. This is also consistent with the findings in the previous study [29] that the decrement in the production is responsible for the flow laminarization. The trend of variation of the turbulent viscous dissipation (figure 10(b))

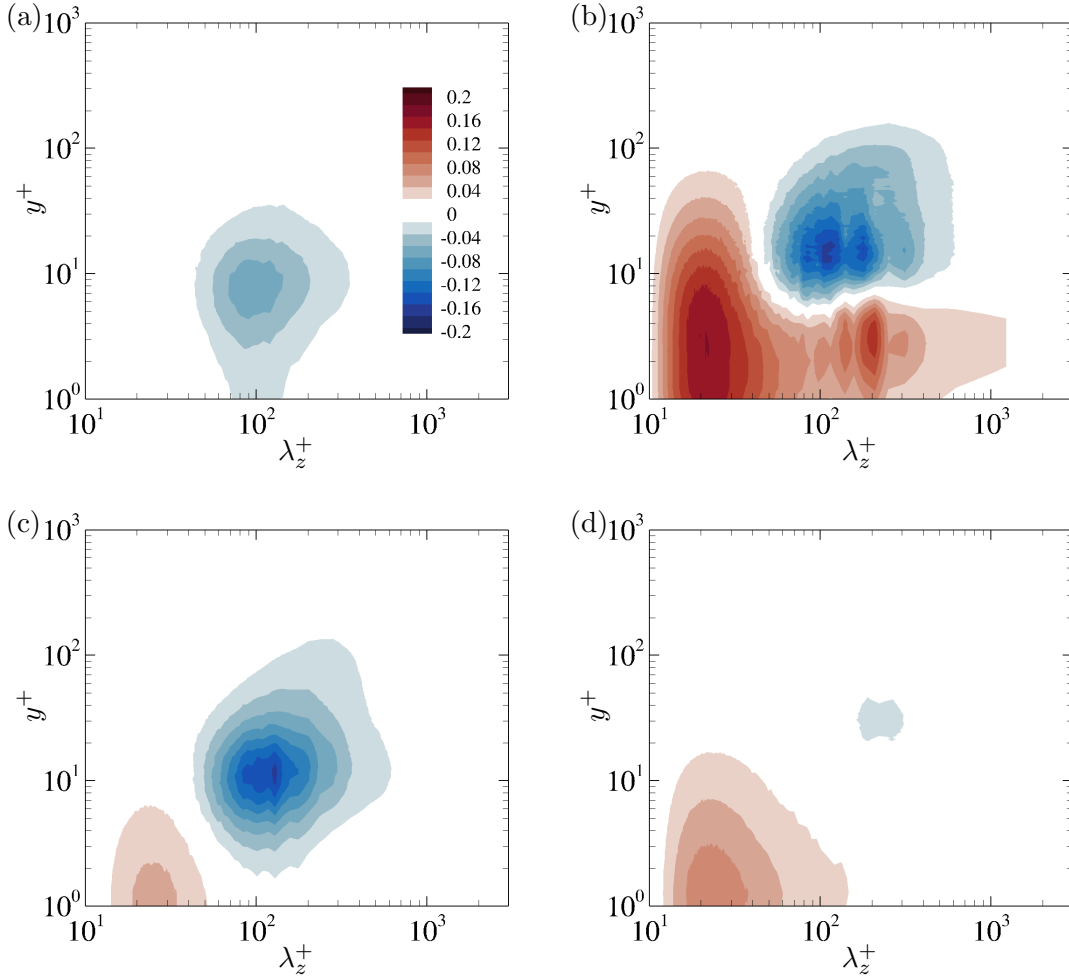


FIG. 11. Pre-multiplied spanwise spectra of the TKE particle force work $k_z E_{F_p, i}^+ u_i'$, (a) case P1-F02, (b) case P1-F06, (c) case P2-F06, (d) case P3-F14.

is similar to the turbulent production, except that the peaks are located at the wall. The work of the particle forces, as shown in figure 10(c), is negative in low mass loading cases and case P2-F06 except for a small region below $y^+ = 3$, indicating that the particles are extracting energy from the fluid. In cases P1-F06 and P3-F14, the region of the positive work extends to $y^+ \approx 10$ and $y^+ \approx 20$, respectively, and as displayed in figure 10(d), this term counteracts approximately 20% and 50% of the viscous dissipation at the wall.

To further illustrate the work of the particle feedback forces on the turbulent kinetic energy in the scale space, in figure 11 we present the pre-multiplied spanwise co-spectra between the particle forces and the velocity fluctuations. For the low mass loading cases (only case P1-F02 is shown in figure 11(a)), the values of the co-spectra are negative, with the peaks located at $y^+ \approx 5$ and $\lambda_z^+ \approx 100$, corresponding to the locations and the spanwise characteristic length scales of the particle streaks. Recalling figure 1(b), we infer that the particles that cluster as velocity streaks are mostly being decelerated, and reversely, feeding back positive forces to the fluid, thereby leading to the negative work when acting on the negative velocity fluctuations. In the previous study of Dritselis and Vlachos [35], it has also been demonstrated via conditional average that the particles

generate the feedback forces and torques that counteract the streamwise vortices in the cross-stream plane. Both of these phenomena point to the elucidation that the negative work of the particles should be ascribed as the reason for the reduction of the turbulent intensities and the more coherent streaky structures in the near-wall region. In cases P1-F06 and P2-F06 with moderate mass loading, the negative regions of the co-spectra are strengthened, with the peaks shifted slightly upwards and towards the larger spanwise scales. Moreover, a small near-wall peak appears at small-scale $\lambda_z^+ \approx 25$ in case P2-F06. In case P1-F06, such positive regions are much more intense in comparison, and cover a much wider range in the wall-normal direction at small scales and in the scale space in the near-wall region. Considering that the peak of the spectra is reached at $y^+ \approx 25$ and $\lambda_z^+ \approx 200$, we conjecture that the intense energy production at small scales and the near-wall region are transferred to such scales by the nonlinear inter-scale transfer and the spatial diffusion. Details are left to be explored in our future work. In case P3-F14, the negative spectra almost disappear, while the near-wall positive spectra intensities are slightly stronger compared with those in case P2-F06. Since there is no obvious small-scale particle clustering in either of these cases, this term can be ascribed to the comparatively discrete particle force distributions, as shown in figure 3(c) the mixed accelerating and decelerating particles without showing obvious spatial separation between them as in other cases.

The works of the forces acting on the particles and the feedback forces acting on the fluid do not add up to zero, as demonstrated by Zhao *et al.* [26]. Specifically, the work of the fluid on a single particle per unit mass writes as

$$w_{fp} = F_{p,i}v_i/m_p = \frac{f_D}{\tau_p}(u_{p,i} - v_i)v_i \quad (19)$$

and reversely that on the particle as

$$w_{pf} = -F_{p,i}u_{p,i}/m_p = -\frac{f_D}{\tau_p}(u_{p,i} - v_i)u_{p,i}, \quad (20)$$

and their summation

$$w_p = w_{fp} + w_{pf} = -\frac{f_D}{\tau_p}(u_{p,i} - v_i)^2 \quad (21)$$

is negative, suggesting that the forces between the fluid and particles dissipate their total kinetic energy, which is referred to as the particle dissipation. In figure 12 (a,b) we present the wall-normal distribution of the mean and fluctuating particle dissipation $w_{p,m}$ and $w_{p,f}$. In general, the latter is higher than the former. The $w_{p,f}$, in particular, is decreasing with both the Stokes number St^+ and the mass loading φ_m . In the integral sense, the particle dissipation on the unit mass of fluid, denoted as $W_{p,m}$ and $W_{p,f}$, is also primarily constituted by the latter, namely the slip velocity fluctuations, as shown in figure 12 (c,d). Both $W_{p,m}$ and $W_{p,f}$ are the most intense near the wall, and under viscous scales, the orders of the magnitudes of these terms are $O(10^{-3})$ and $O(10^{-4})$, respectively, suggesting their relatively small contribution compared with the mean kinetic energy dissipation. Compared with the turbulent kinetic energy viscous dissipation, $W_{p,f}$

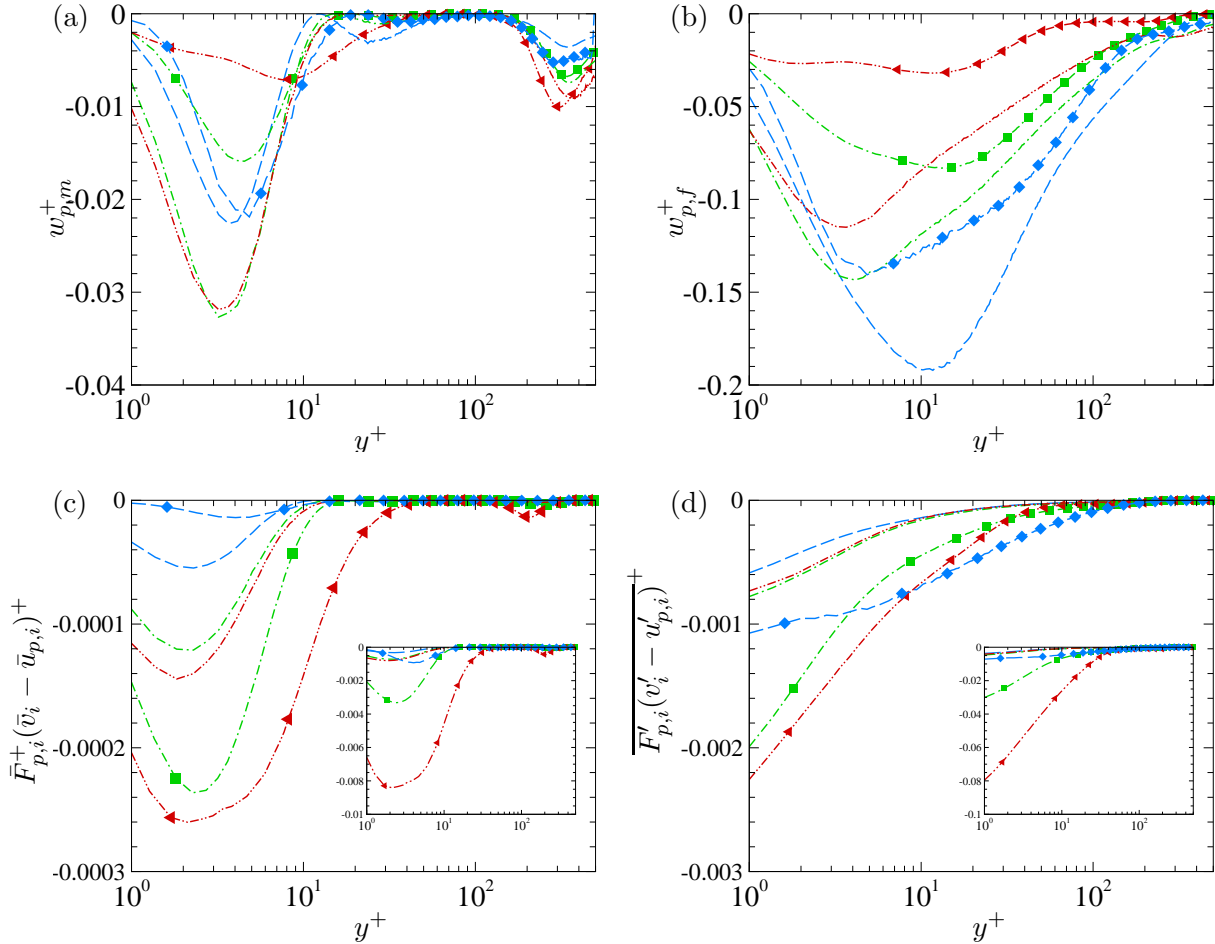


FIG. 12. Particle force dissipation (a) $w_{p,m}^+$, (b) $w_{p,f}^+$, (c) $\bar{F}_{p,m}^+$, (d) $\bar{F}_{p,f}^+$, insets of (c,d): normalized by wall viscous dissipation ε_w . Line legends refer to Table I.

constitute finitely of approximately 8% at the wall in case P3-F14 and less than 3% in case P2-F06 and less than 1% in other cases.

The particle dissipation reflects the kinetic energy loss due to the particle-fluid interaction which, if only the drag force is considered, is produced due to the fluid viscosity. Therefore, in the cases where the heat exchanges between the fluid and the particles are incorporated, namely the two-way force and heat coupling, the particle dissipation should be added either to the internal/total energy equation of particles or fluid, or both, depending on the type of particles considered, otherwise there will be total energy loss in such particulate systems.

E. Mean temperature

Lastly, we discuss the two-way coupling effects on the mean temperature, as shown in figure 13(a). Compared with the one-way coupling case, the mean temperature is not much affected in the cases with low particle mass loadings and case P1-F06. In moderate and high mass loading cases P2-F06 and P3-F14, however, the mean temperature is

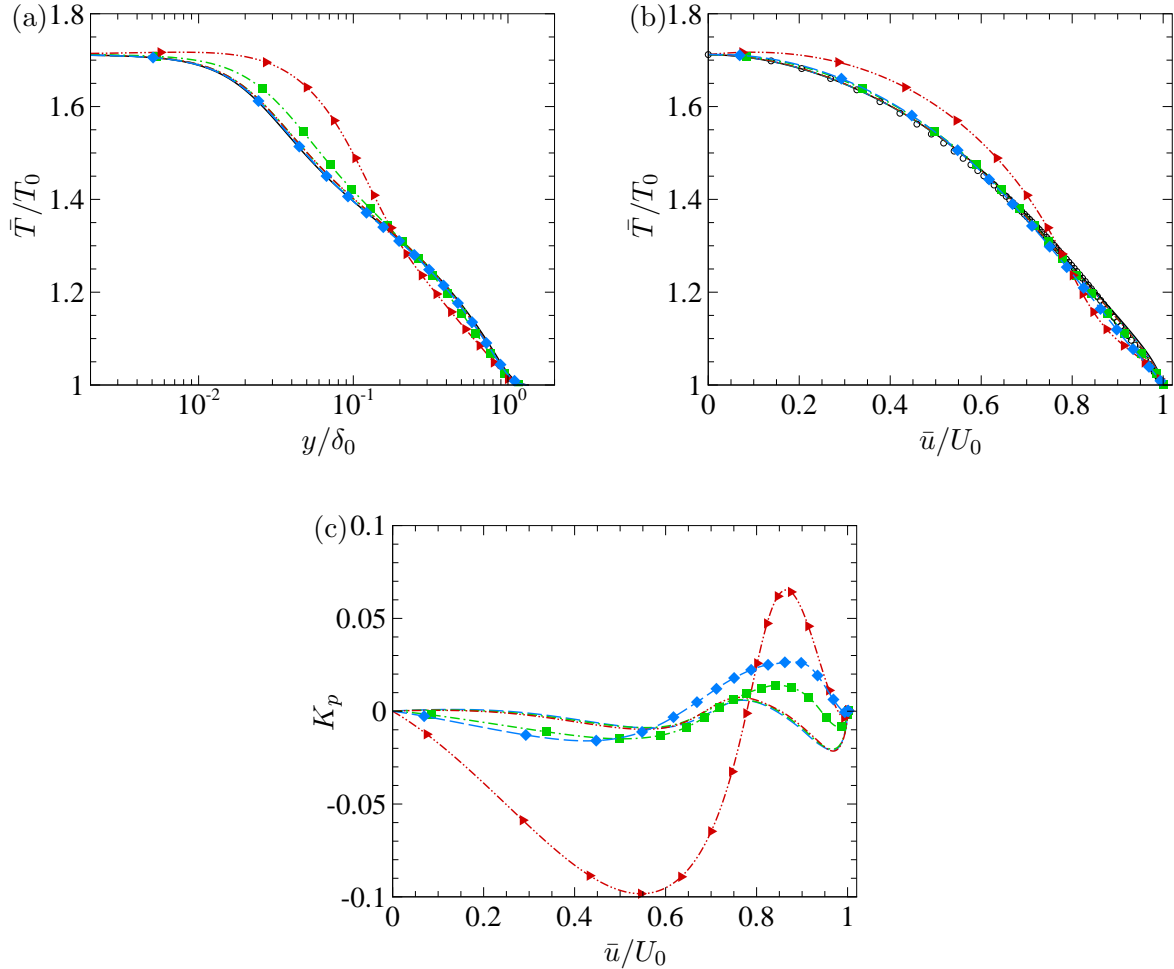


FIG. 13. Mean temperature distribution, (a) \bar{T}/T_0 against y , (b) \bar{T}/T_0 against \bar{u} and (c) compensating kinetic energy K_p . Line legends refer to Table I, black circles in (b): GRA in equation (22).

augmented near the wall below $y = 0.2\delta_0$ while abated above that location. This leads to the disparity from the generalized Reynolds analogy (GRA) [53], which is written as

$$\frac{\bar{T}}{T_0} = \frac{\bar{T}_w}{T_0} + \frac{T_{rg} - T_w}{T_0} \frac{\bar{u}}{U_0} + \frac{T_\infty - T_{rg}}{T_0} \left(\frac{\bar{u}}{U_0} \right) \quad (22)$$

with the generalized recovery temperature $T_{rg} = T_0 + r_g U_0^2 / (2C_p)$ and r_g the generalized recovery coefficient. Obviously, in the case of canonical compressible wall-bounded turbulence, the mean temperature is a quadratic function of the mean velocity, dependent on the wall temperature and the free-stream Mach numbers. As illustrated in figure 13(b), this is approximately the case for low and moderate particle mass loadings, but evidently not for the high mass loading case P3-F14.

The differences from the GRA have also been found in our previous studies regarding the compressible turbulent boundary layers subject to wall disturbances [62–64], where the deviation of the relation between the mean temperature and mean velocity can be ascribed to the disparities in the boundary conditions. For the presently considered cases,

however, such deviations should be attributed to the particle feedback forces. We start from the resemblance between the mean momentum and total enthalpy equations. Under the assumption of $Pr = 1$, the mean momentum and total enthalpy equations can be approximately cast as

$$\bar{\rho}\bar{u}_1\frac{\partial\bar{u}_1}{\partial x} + \bar{\rho}\bar{u}_2\frac{\partial\bar{u}_1}{\partial y} \approx \frac{\partial}{\partial y} \left(\bar{\mu}\frac{\partial\bar{u}_1}{\partial y} - \overline{\rho u_1'' u_2''} \right) + \bar{F}_{p,1} \quad (23)$$

$$\bar{\rho}\bar{u}_1\frac{\partial\bar{H}}{\partial x} + \bar{\rho}\bar{u}_2\frac{\partial\bar{H}}{\partial y} \approx \frac{\partial}{\partial y} \left(\bar{\mu}\frac{\partial\bar{H}}{\partial y} - \overline{\rho H' u_2''} \right) + \bar{F}_{p,1}\bar{u}_1. \quad (24)$$

with the streamwise Reynolds stress and viscous stress neglected. Multiplying the former by U_w and subtracting it from the latter, we have

$$\left(\bar{\rho}\bar{u}_1\frac{\partial}{\partial x} + \bar{\rho}\bar{u}_2\frac{\partial}{\partial y} - \frac{\partial}{\partial y} \left(\bar{\mu}\frac{\partial}{\partial y} \right) \right) (\bar{H} - U_w\bar{u}) = \bar{F}_{p,1}(\bar{u}_1 - U_w). \quad (25)$$

In the cases without particle feedback forces, the right-hand-side is zero, then we have the solution

$$\bar{H} - \bar{H}_w = U_w\bar{u}. \quad (26)$$

Here, H_w is the total enthalpy at the wall and $U_w = -Prq_{yw}/\tau_w$. Zhang *et al.* [53] further suggested that $\bar{H}_g = C_p T + r_g \bar{u}_1^2/2$ should be used instead of \bar{H} to incorporate the non-unity of Pr . This gives the GRA above in equation (22).

If the right-hand-side term is non-negligible, the generalized total enthalpy \bar{H}_g should be further expressed as

$$\bar{H}_g = C_p T + r_g \bar{u}_1^2/2 + K_p, \quad (27)$$

where K_p represents the kinetic energy transported by particles, hereinafter referred to as the compensating kinetic energy. The K_p is a solution of the following equation

$$\left(\bar{\rho}\bar{u}_1\frac{\partial}{\partial x} + \bar{\rho}\bar{u}_2\frac{\partial}{\partial y} - \frac{\partial}{\partial y} \left(\bar{\mu}\frac{\partial}{\partial y} \right) \right) K_p = \bar{F}_{p,1}(\bar{u}_1 - U_w), \quad (28)$$

but it cannot be easily solved because the operator on the left-hand-side also depends on the particle feedback force on the right-hand-side. Statistically, we can obtain the K_p by subtracting the original GRA from the DNS results, as is shown in figure 11(c). It is negative in the inner region and positive in the outer region, corresponding to the influences of the kinetic energy transfer between the particles and the fluid.

The compensating kinetic energy K_p is by definition the kinetic energy loss caused by the particle forces. This can also be supported by their same trend of variation along the wall-normal direction (comparing figures 13(c) and 12(d)). The transport of the kinetic energy suggests that the work of the particle forces is balanced by the viscous dissipation, which transfers the kinetic energy to the internal energy, thus leading to the increment of the local temperature. From another perspective, in the cases where near-wall turbulence remains active, the vertical turbulent heat flux further redistributes the internal energy, rendering the mean temperature-velocity relation similar to the canonical compressible turbulent boundary layers. On the contrary, in high mass loading cases

where the near-wall turbulence is laminarized, the high temperature close to the wall cannot be transported towards the free-stream. These factors could probably synergize, resulting in a higher temperature in the near-wall region.

IV. CONCLUSIONS

In the current investigation, we conducted direct numerical simulations of particle-laden compressible turbulent boundary layers at a free-stream Mach number of 2.0. We focused on the two-way force coupling between the particles and the fluid, particularly examining how particles modulate momentum and kinetic energy transfer across various mass loadings and particle Stokes numbers.

The presence of particles leads to a suppression of turbulence and laminarization, characterized not only by weaker, wider, and more coherent velocity streaks but also by reductions in skin friction, turbulent kinetic energy, and Reynolds shear stress. The extent of turbulence suppression is primarily dependent on the mass loadings, but also on the particle Stokes number, which influences the preferential accumulation and clustering of particles near the wall. In cases of the highest mass loading examined in this study, near-wall turbulence is entirely laminarized. The remnant turbulent fluctuations are induced by particles that are swept down from the outer region.

The analysis of mean momentum transfer and skin friction decomposition reveals that the presence of particles minimally affects viscous shear stress. However, the contribution from Reynolds stress diminishes while that from particle feedback force escalates with increasing mass loading. Through skin friction decomposition, it was observed that the aggregate of terms, excluding the particle feedback force, transitions from a turbulent empirical relationship to a laminar one as mass loading increases.

The distributions of turbulent kinetic energy and pre-multiplied spanwise spectra conclusively demonstrate that moderate mass loadings disrupt near-wall turbulence, exhibiting a broader characteristic spanwise length scale at elevated wall-normal positions. In the case with high mass loading, near-wall turbulence is entirely eradicated. Analysis of turbulent kinetic energy transport indicates significant suppression of both production and dissipation, with particle-induced work predominating the production of turbulent kinetic energy in the near-wall region and at smaller scales for moderate and high mass loadings. Particle dissipation, induced by the interaction between particles and fluid due to viscosity, is substantial relative to viscous dissipation and merits consideration in simulations involving two-way force and heat coupling. Additionally, it was found that the mean temperature is elevated in the near-wall region and reduced in the outer region in cases of high mass loading, attributable to particle feedback forces and the diminution of near-wall turbulent motions.

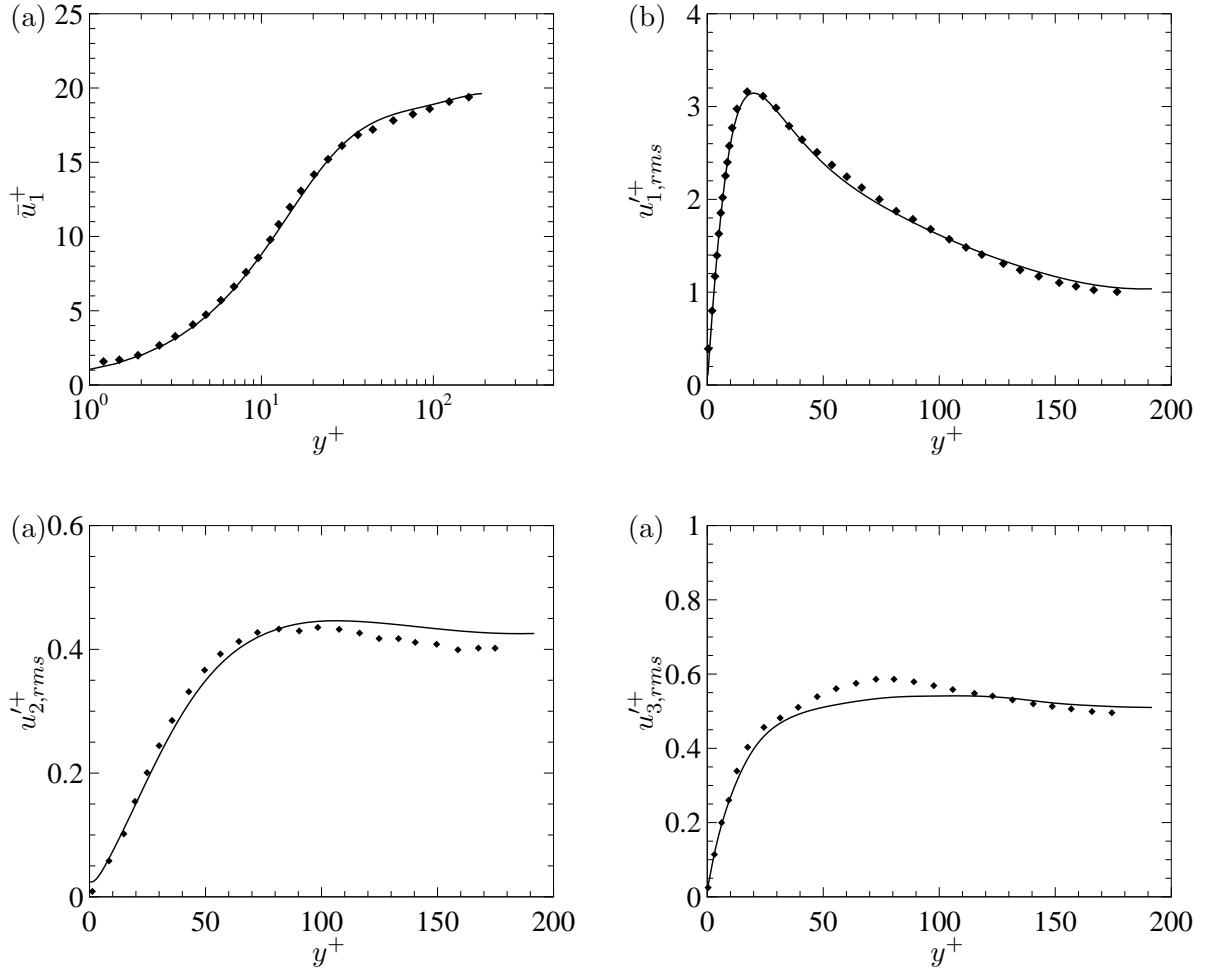


FIG. 14. Wall-normal distribution of the (a) mean velocity \bar{u}_1^+ and (b) $u'_{1,rms}^+$, (c) $u'_{2,rms}^+$, (d) $u'_{3,rms}^+$. Lines: present simulation, symbols: reported by Zhao *et al.* [30].

Appendix A: Validation of the numerical solver

We validate our two-way coupling particle-laden compressible turbulence solver by performing direct numerical simulations for turbulent channel flows at the bulk Mach number $M_b = u_b/a_w = 0.5$ and friction Reynolds number $Re_\tau = \rho_w u_\tau h \approx 180$, with u_b the bulk velocity, a_w the acoustic velocity at the wall and h the half channel height. The turbulence is monitored to be temporally fully developed before 4×10^6 particles with the diameters of $d_p = 0.004h$ and the density ratio $\rho_p = 1042\rho_b$ (ρ_b is the fluid bulk density) are randomly injected into the channel with the size of $12h$, $2h$ and $6h$ in the streamwise, wall-normal and spanwise directions. The particle Stokes number St^+ is approximately 30 and the mass loading is $\varphi_m \approx 1.0$.

We compare our simulation results with those reported by Zhao *et al.* [30], as shown in Figure 14. Both the mean velocity and the root-mean-square of the velocity fluctuations collapse well with the reference data, proving our numerical solver valid.

-
- [1] G. Rudinger, *Fundamentals of gas particle flow*, Vol. 2 (Elsevier, 2012).
- [2] X. Cheng, Q. Zeng, and F. Hu, Stochastic modeling the effect of wind gust on dust entrainment during sand storm, *Chin. Sci. Bull* **57**, 3595 (2012).
- [3] H. Liu and X. Zheng, Large-scale structures of wall-bounded turbulence in single-and two-phase flows: advancing understanding of the atmospheric surface layer during sandstorms, *Flow* **1**, E5 (2021).
- [4] E. Saw, R. Shaw, S. Ayyalasomayajula, P. Chuang, and A. Gylfason, Inertial clustering of particles in high-Reynolds-number turbulence, *Phys. Rev. Lett.* **100**, 214501 (2008).
- [5] A. Soldati and C. Marchioli, Physics and modelling of turbulent particle deposition and entrainment: Review of a systematic study, *Int. J. Multiph. Flow* **35**, 827 (2009).
- [6] M. Kuerten, Point-particle DNS and LES of particle-laden turbulent flow—a state-of-the-art review, *Flow Turbul. Combust.* **97**, 689 (2016).
- [7] S. Balachandar and J. Eaton, Turbulent dispersed multiphase flow, *Annu. Rev. Fluid Mech.* **42**, 111 (2010).
- [8] L. Brandt and F. Coletti, Particle-laden turbulence: progress and perspectives, *Annu. Rev. Fluid Mech.* **54**, 159 (2022).
- [9] Y. Cao, Z. Wu, and Z. Xu, Effects of rainfall on aircraft aerodynamics, *Prog. Aerosp. Sci.* **71**, 85 (2014).
- [10] E. Loth, J. Tyler Daspit, M. Jeong, T. Nagata, and T. Nonomura, Supersonic and hypersonic drag coefficients for a sphere, *AIAA J.* **59**, 3261 (2021).
- [11] A. Vreman, Turbulence characteristics of particle-laden pipe flow, *J. Fluid Mechanics* **584**, 235 (2007).
- [12] Z. Li, Z. Cui, L. Zhao, N. Hussain, Y. Zhao, C. Yang, X. Jiang, L. Li, J. Song, B. Zhang, Z. Cheng, and H. Wu, High-throughput production of kilogram-scale nanofibers by Kármán vortex solution blow spinning, *Sci. Adv.* **8**, eabn3690 (2022).
- [13] W. Xiao, T. Jin, K. Luo, Q. Dai, and J. Fan, Eulerian–Lagrangian direct numerical simulation of preferential accumulation of inertial particles in a compressible turbulent boundary layer, *J. Fluid Mech.* **903**, A19 (2020).
- [14] P. Wang, B. Zhou, and X. Zheng, Turbophoresis and preferential accumulation of inertial particles in compressible turbulent channel flow: Effect of Mach number, *Phys. Rev. Fluids* **9**, 034305 (2024).
- [15] D. Rouson and J. Eaton, On the preferential concentration of solid particles in turbulent channel flow, *J. Fluid Mech.* **428**, 149 (2001).
- [16] G. Sardina, P. Schlatter, L. Brandt, F. Picano, and C. M. Casciola, Wall accumulation and spatial localization in particle-laden wall flows, *J. Fluid Mech.* **699**, 50 (2012).
- [17] A. Soldati, Particles turbulence interactions in boundary layers, *Appl. Math. Mech.* **85**, 683 (2005).
- [18] C. Narayanan, D. Lakehal, L. Botto, and A. Soldati, Mechanisms of particle deposition in

- a fully developed turbulent open channel flow, *Phys. Fluids* **15**, 763 (2003).
- [19] M. Picciotto, C. Marchioli, and A. Soldati, Characterization of near-wall accumulation regions for inertial particles in turbulent boundary layers, *Phys. Fluids* **17**, 098101 (2005).
- [20] M. Bernardini, Reynolds number scaling of inertial particle statistics in turbulent channel flows, *J. Fluid Mech.* **758**, R1 (2014).
- [21] B. Milici and M. de Marchis, Statistics of inertial particle deviation from fluid particle trajectories in horizontal rough wall turbulent channel flow, *Int. J. Heat Fluid Flow* **60**, 1 (2016).
- [22] M. Bernardini, S. Pirozzoli, and P. Orlandi, The effect of large-scale turbulent structures on particle dispersion in wall-bounded flows, *Int. J. Multiph. flow* **51**, 55 (2013).
- [23] Y. Jie, Z. Cui, C. Xu, and L. Zhao, On the existence and formation of multi-scale particle streaks in turbulent channel flows, *J. Fluid Mech.* **935**, A18 (2022).
- [24] Y. Motoori, C. Wong, and S. Goto, Role of the hierarchy of coherent structures in the transport of heavy small particles in turbulent channel flow, *J. Fluid Mech.* **942**, A3 (2022).
- [25] J. Eaton, Two-way coupled turbulence simulations of gas-particle flows using point-particle tracking, *Int. J. Multiph. Flow* **35**, 792 (2009).
- [26] L. Zhao, H. Andersson, and J. Gillissen, Interphasial energy transfer and particle dissipation in particle-laden wall turbulence, *J. Fluid Mech.* **715**, 32 (2013).
- [27] Q. Pan, H. Xiang, Z. Wang, H. Andersson, and L. Zhao, Kinetic energy balance in turbulent particle-laden channel flow, *Phys. Fluids* **32** (2020).
- [28] D. Richter and P. Sullivan, Momentum transfer in a turbulent, particle-laden Couette flow, *Phys. Fluids* **25** (2013).
- [29] P. Muramulla, A. Tyagi, P. Goswami, and V. Kumaran, Disruption of turbulence due to particle loading in a dilute gas-particle suspension, *J. Fluid Mech.* **889**, A28 (2020).
- [30] L. Zhao, H. Andersson, and J. Gillissen, Turbulence modulation and drag reduction by spherical particles, *Phys. Fluids* **22** (2010).
- [31] J. Kulick, J. Fessler, and J. Eaton, Particle response and turbulence modification in fully developed channel flow, *J. Fluid Mech.* **277**, 109 (1994).
- [32] Y. Li, J. McLaughlin, K. Kontomaris, and L. Portela, Numerical simulation of particle-laden turbulent channel flow, *Phys. Fluids* **13**, 2957 (2001).
- [33] C. Dritselis, Direct numerical simulation of particle-laden turbulent channel flows with two- and four-way coupling effects: budgets of Reynolds stress and streamwise enstrophy, *Fluid Dyn. Res* **48**, 015507 (2016).
- [34] D. Richter, Turbulence modification by inertial particles and its influence on the spectral energy budget in planar Couette flow, *Phys. Fluids* **27** (2015).
- [35] C. Dritselis and N. Vlachos, Numerical study of educed coherent structures in the near-wall region of a particle-laden channel flow, *Phys. Fluids* **20** (2008).
- [36] L. Mortimer and M. Fairweather, Density ratio effects on the topology of coherent turbulent structures in two-way coupled particle-laden channel flows, *Phys. Fluids* **32**, 103302 (2020).
- [37] Z. Wu, J. Wu, B. Wang, and Z. Lu, Effect of Stokes number on energy modulation of the

- fluid in turbulent particle-laden channel flows, *J. Hydrodynam.* **34**, 510 (2022).
- [38] J. Lee and C. Lee, Modification of particle-laden near-wall turbulence: Effect of Stokes number, *Phys. Fluids* **27** (2015).
- [39] C. Dritselis and N. Vlachos, Numerical investigation of momentum exchange between particles and coherent structures in low Re turbulent channel flow, *Phys. Fluids* **23** (2011).
- [40] D. Richter and P. Sullivan, Modification of near-wall coherent structures by inertial particles, *Phys. Fluids* **26** (2014).
- [41] G. Wang and D. Richter, Modulation of the turbulence regeneration cycle by inertial particles in planar Couette flow, *J. Fluid Mech.* **861**, 901 (2019).
- [42] H. Nasr, G. Ahmadi, and J. McLaughlin, A dns study of effects of particle–particle collisions and two-way coupling on particle deposition and phasic fluctuations, *J. Fluid Mech.* **640**, 507 (2009).
- [43] T. Zhou, L. Zhao, W. Huang, and C. Xu, Non-monotonic effect of mass loading on turbulence modulations in particle-laden channel flow, *Phys. Fluids* **32** (2020).
- [44] Y. Yang, J. Wang, Y. Shi, Z. Xiao, X. He, and S. Chen, Interactions between inertial particles and shocklets in compressible turbulent flow, *Phys. Fluids* **26** (2014).
- [45] Q. Zhang, H. Liu, Z. Ma, and Z. Xiao, Preferential concentration of heavy particles in compressible isotropic turbulence, *Phys. Fluids* **28**, 055104 (2016).
- [46] Q. Dai, K. Luo, T. Jin, and J. Fan, Direct numerical simulation of turbulence modulation by particles in compressible isotropic turbulence, *J. Fluid Mech.* **832**, 438 (2017).
- [47] Q. Dai, T. Jin, K. Luo, and J. Fan, Direct numerical simulation of particle dispersion in a three-dimensional spatially developing compressible mixing layer, *Phys. Fluids* **30**, 113301 (2018).
- [48] Q. Dai, T. Jin, K. Luo, and J. Fan, Direct numerical simulation of a three-dimensional spatially evolving compressible mixing layer laden with particles. I. Turbulent structures and asymmetric properties, *Phys. Fluids* **31** (2019).
- [49] Q. Dai, T. Jin, K. Luo, W. Xiao, and J. Fan, Direct numerical simulation of a three-dimensional spatially evolving compressible mixing layer laden with particles. II. Turbulence anisotropy and growth rate, *Phys. Fluids* **31**, 083303 (2019).
- [50] G. Chen, H. Wang, K. Luo, and J. Fan, Two-way coupled turbulent particle-laden boundary layer combustion over a flat plate, *Journal of Fluid Mechanics* **948**, A12 (2022).
- [51] M. Yu, L. Zhao, X. Yuan, and C. Xu, Transport of inertial spherical particles in compressible turbulent boundary layers, *arXiv preprint arXiv:2401.01157* (2024).
- [52] A. Musker, Explicit expression for the smooth wall velocity distribution in a turbulent boundary layer, *AIAA J.* **17**, 655 (1979).
- [53] Y. Zhang, W. Bi, F. Hussain, and Z. She, A generalized Reynolds analogy for compressible wall-bounded turbulent flows, *J. Fluid Mech.* **739**, 392 (2014).
- [54] M. Klein, A. Sadiki, and J. Janicka, A digital filter based generation of inflow data for spatially developing direct numerical or large eddy simulations, *J. Comput. Phys.* **186**, 652 (2003).

- [55] M. Bernardini, D. Modesti, F. Salvatore, and S. Pirozzoli, STREAMS: A high-fidelity accelerated solver for direct numerical simulation of compressible turbulent flows, *Comput. Phys. Commun.* **263**, 107906 (2021).
- [56] S. Pirozzoli, Generalized conservative approximations of split convective derivative operators, *J. Comput. Phys.* **229**, 7180 (2010).
- [57] S. Pirozzoli, Numerical methods for high-speed flows, *Annu. Rev. Fluid Mech.* **43**, 163 (2011).
- [58] A. Wray, Minimal storage time advancement schemes for spectral methods, NASA Ames Research Center, California, Report No. MS **202** (1990).
- [59] S. Pirozzoli and M. Bernardini, Turbulence in supersonic boundary layers at moderate Reynolds number, *J. Fluid Mech.* **688**, 120 (2011).
- [60] E. Hopkins and M. Inouye, An evaluation of theories for predicting turbulent skin friction and heat transfer on flat plates at supersonic and hypersonic Mach numbers, *AIAA J.* **9**, 993 (1971).
- [61] C. Wenzel, T. Gibis, and M. Kloker, About the influences of compressibility, heat transfer and pressure gradients in compressible turbulent boundary layers, *J. Fluid Mech.* **930**, A1 (2022).
- [62] M. Yu, P. Liu, Z. Tang, X. Yuan, and C. Xu, Effects of wall disturbances on the statistics of supersonic turbulent boundary layers, *Phys. Fluids* **35** (2023).
- [63] M. Yu, Q. Zhou, S. Dong, X. Yuan, and C. Xu, Compressibility effects in supersonic and hypersonic turbulent boundary layers subject to wall disturbances, *J. Fluid Mech.* **972**, A32 (2023).
- [64] M. Yu, B. Li, Q. Zhou, D. Sun, and X. Yuan, Turbulent heat flux and wall heat transfer in hypersonic turbulent boundary layers with wall disturbances, *Aerosp. Sci. Technol.* **145**, 108879 (2024).